C-H hydrogen bond and halogen bond directed self-assembly of ethereal podands and C-X···F^-/HF_2^- halogen bonding in solution

Dipjyoti Dutta,[a] Anamika Gogoi,[a] Rupjyoti Dutta,[a,b] Sarvesh S. Harmalkar,[c,d] Prem Lama,*[b,e] Sandeep Kumar Dey,*[a,b]

[a]*Materials Science and Technology Division, CSIR-North East Institute of Science and Technology, Jorhat, Assam 785006, India. E*mail: sandeep@neist.res.in

[b]*Academy of Scientific and Innovative Research, Ghaziabad, Uttar Pradesh 201002, India*.

[c]*School of Chemical Sciences, Goa University, Taleigao Plateau, Goa 403206, India.*

[d]*Department of Chemistry, Government College Khandola, Goa 403107, India.*

[e]*Distillate and Heavy Oil Processing Division, CSIR-Indian Institute of Petroleum, Mohkampur, Dehradun, Uttarakhand 248005, India. Email: prem.lama@iip.res.in*

1. Materials and experimental methods

All reagents and solvents were obtained from commercial sources and used as received without further purification. Mesitylene, paraformaldehyde, 4-halophenols, 2-halophenols, 2,4-dihalophenols, 4-cyanophenol and quaternary ammonium salts were purchased from either Sigma-Aldrich or Alfa-Aesar chemicals. Solvents (analytical grade), glacial acetic acid and hydrobromic acid for synthesis and crystallization experiments were purchased from CDH chemicals (India) and used without further purification.

^{1}H-NMR and ^{19}F-NMR spectra were recorded on a Bruker Advance FT-400 MHz instrument and chemical shifts were recorded in parts per million (ppm) on the scale using the residual solvent peak as a reference and ^{13}C spectra were obtained at 100 MHz at 298 K. Powder X-ray diffraction patterns of dried crystalline powder were recorded using a Bruker-D8 Advance X-ray diffractometer with Cu-K_α radiation at λ = 0.15418 nm. Bruker D8 Quest ECO single crystal X-ray diffractometer was used for data collection at 298 K. Thermogravimetric analysis was carried out using an FTA 449 F3 Jupiter instrument under nitrogen atmosphere.

2. Characterization of podands by NMR spectroscopy

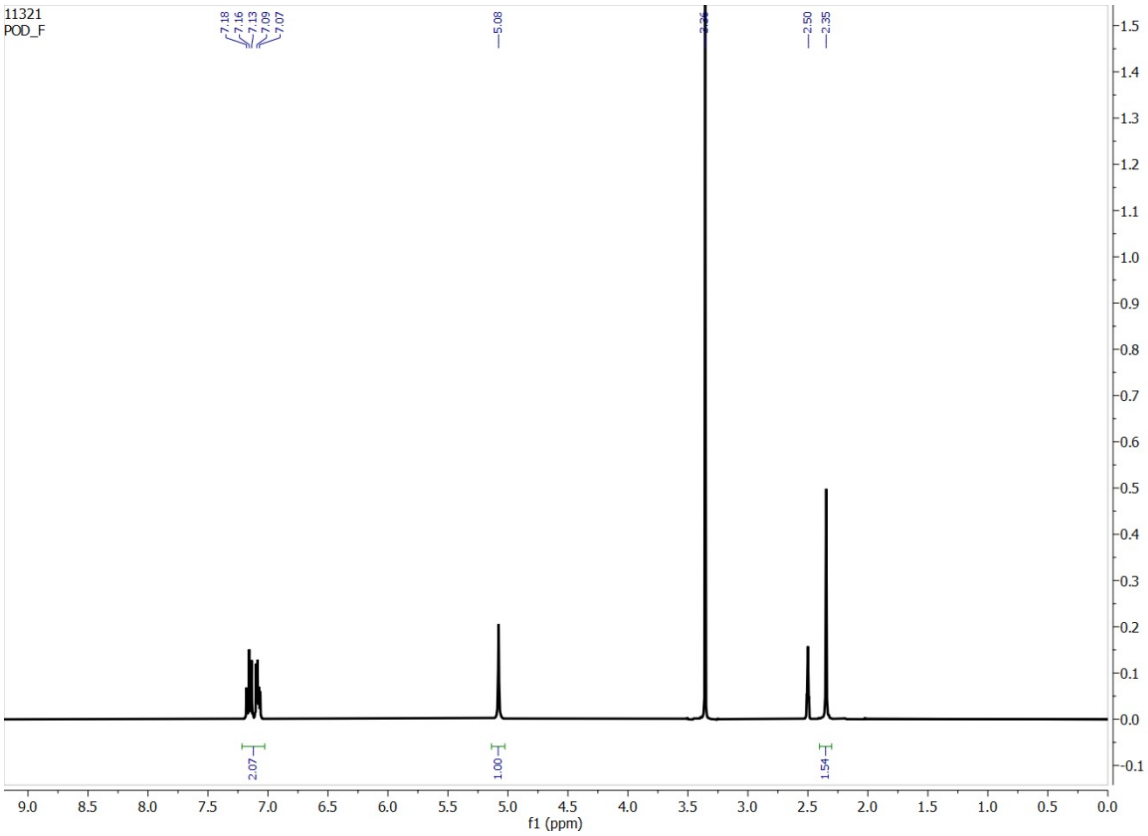

Fig. S1. ^{1}H-NMR spectrum of **P1** in DMSO-D_6.

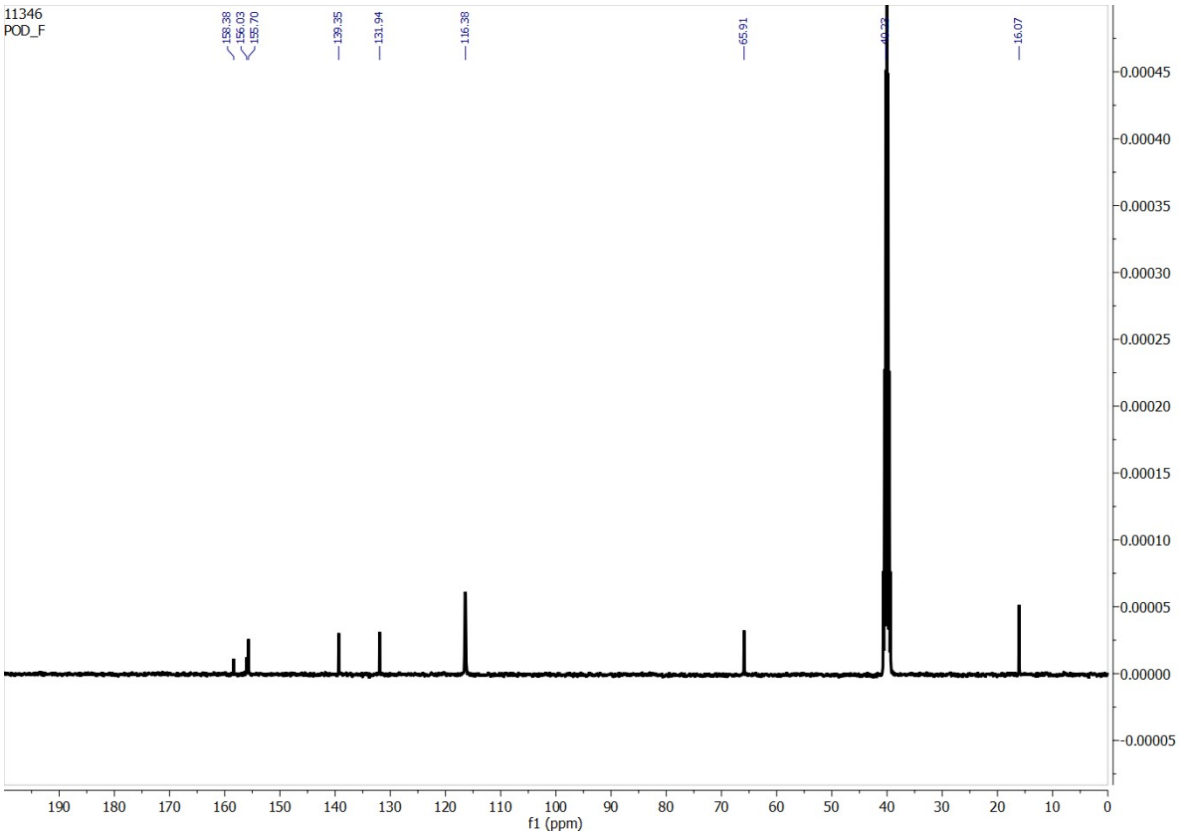

Fig. S2. ^{13}C-NMR spectrum of **P1** in DMSO-D_6.

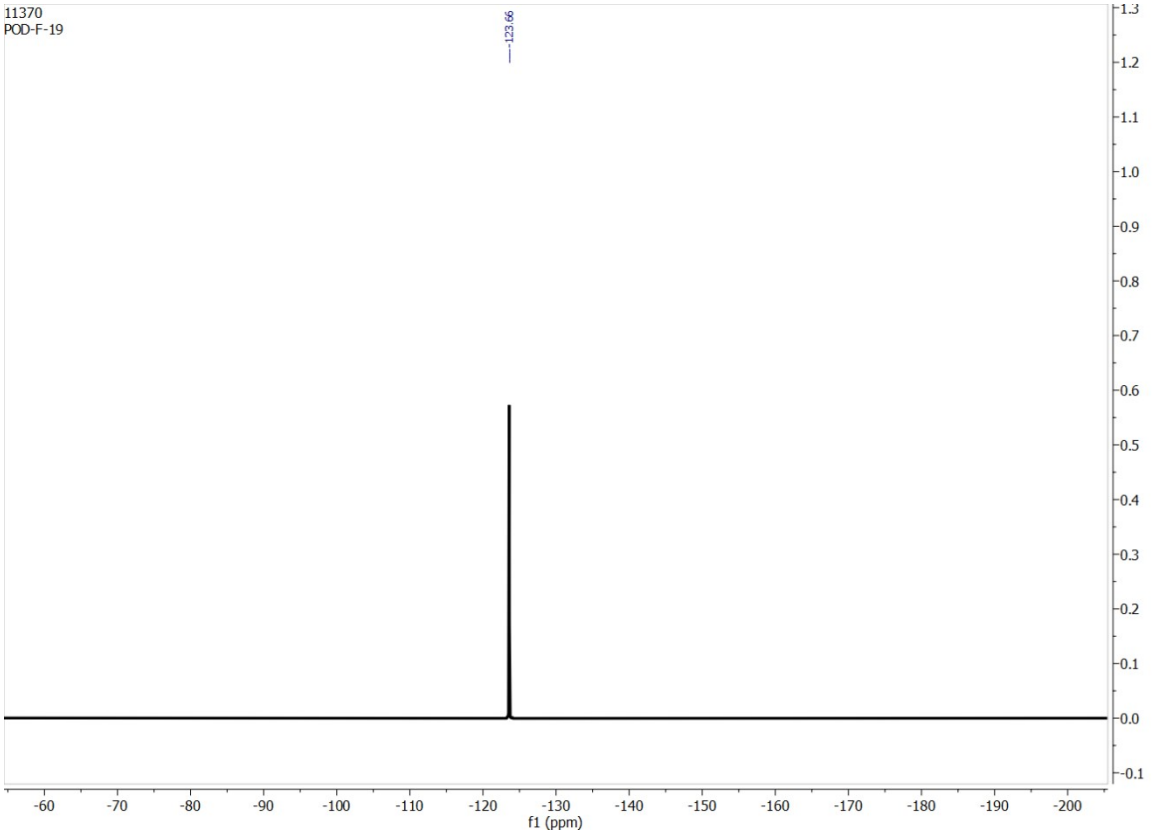

Fig. S3. ^{19}F-NMR spectrum of **P1** in DMSO-D_6.

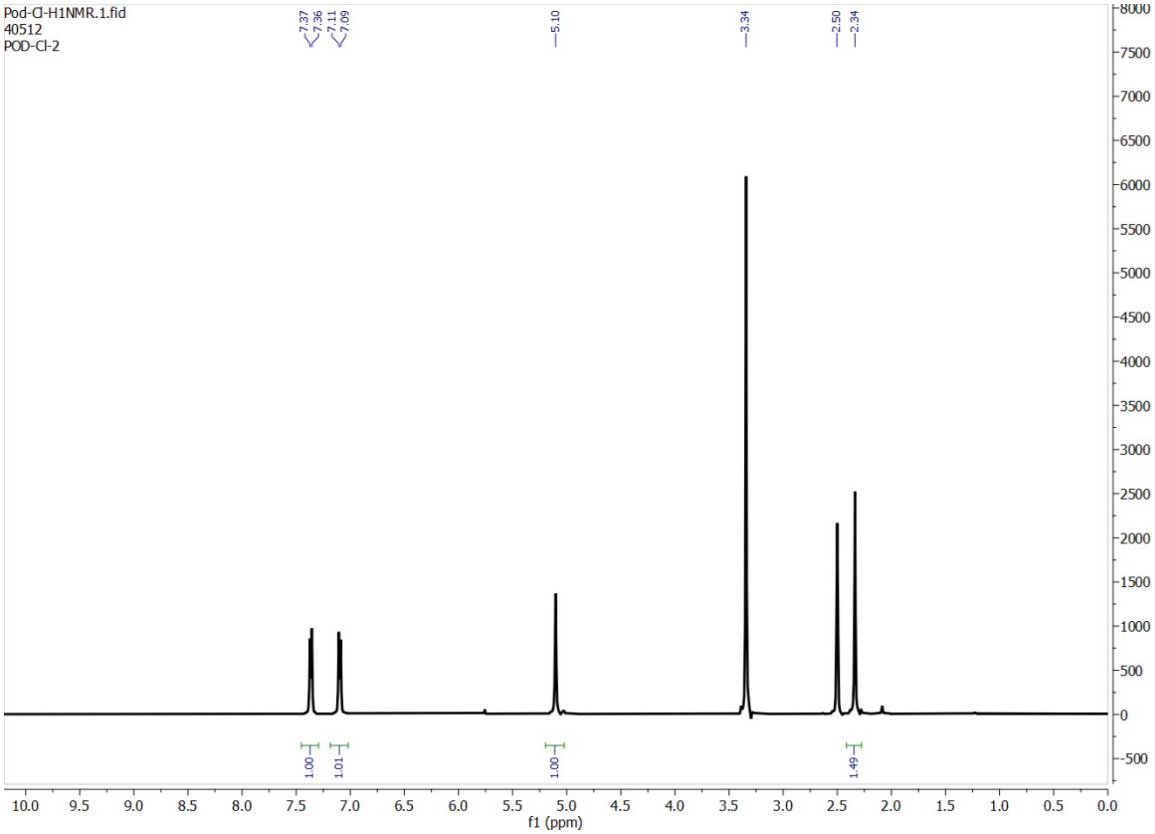

Fig. S4. ^{1}H-NMR spectrum of **P2** in DMSO-D_6.

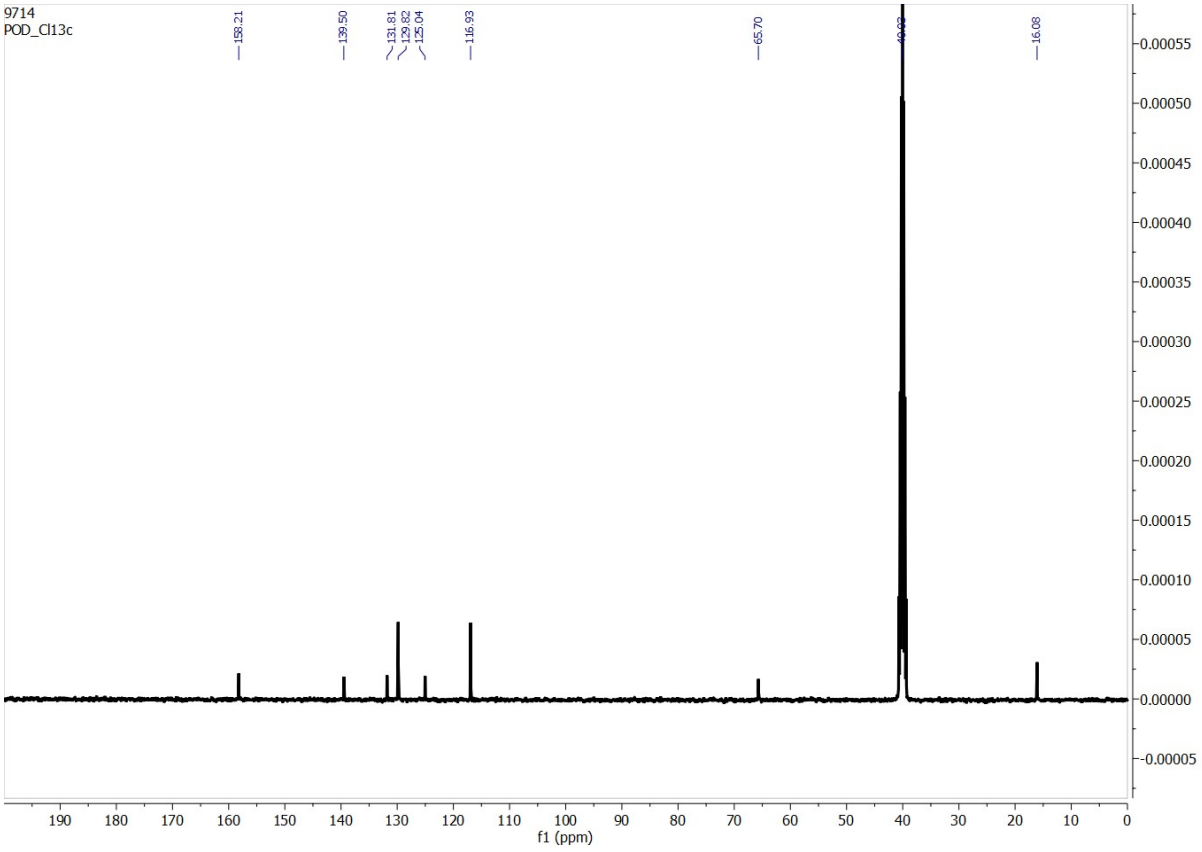

Fig. S5. ^{13}C-NMR spectrum of **P2** in DMSO-D_6.

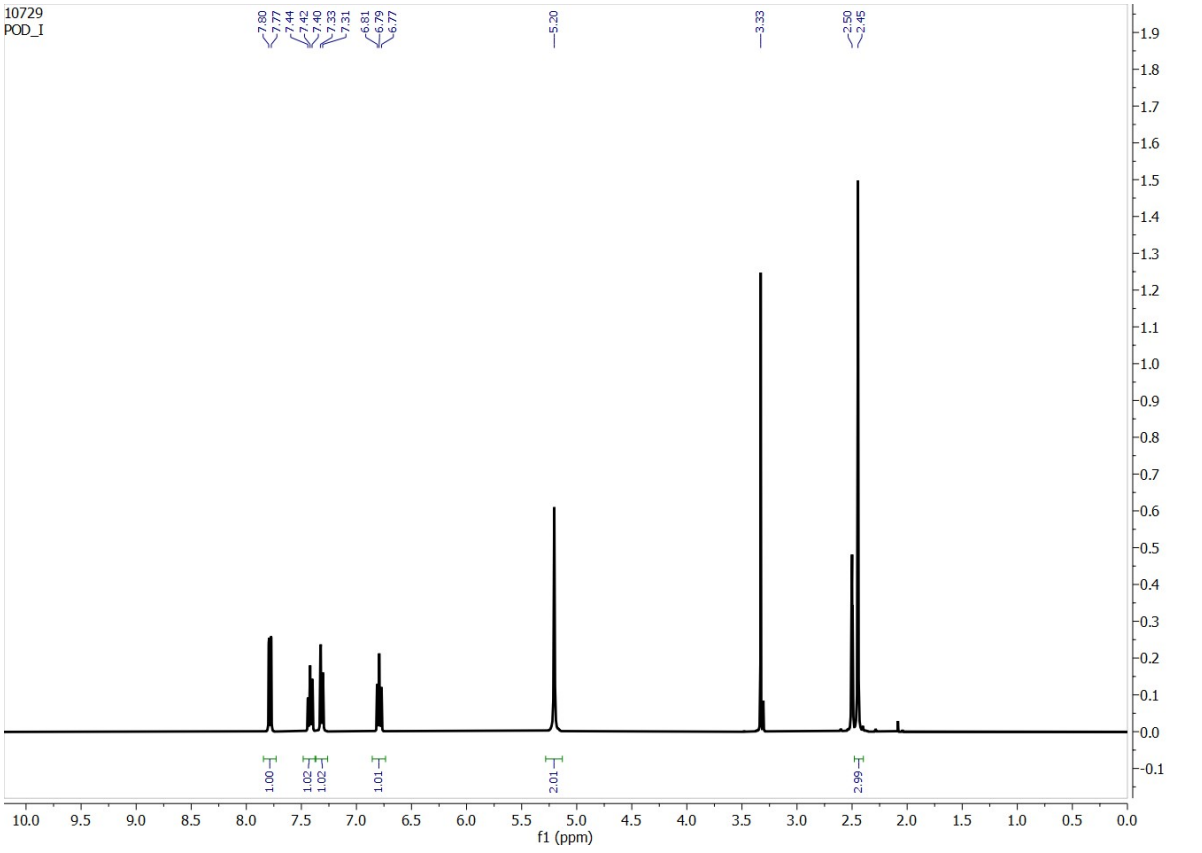

Fig. S6. ^{1}H-NMR spectrum of **P5** in DMSO-D_6.

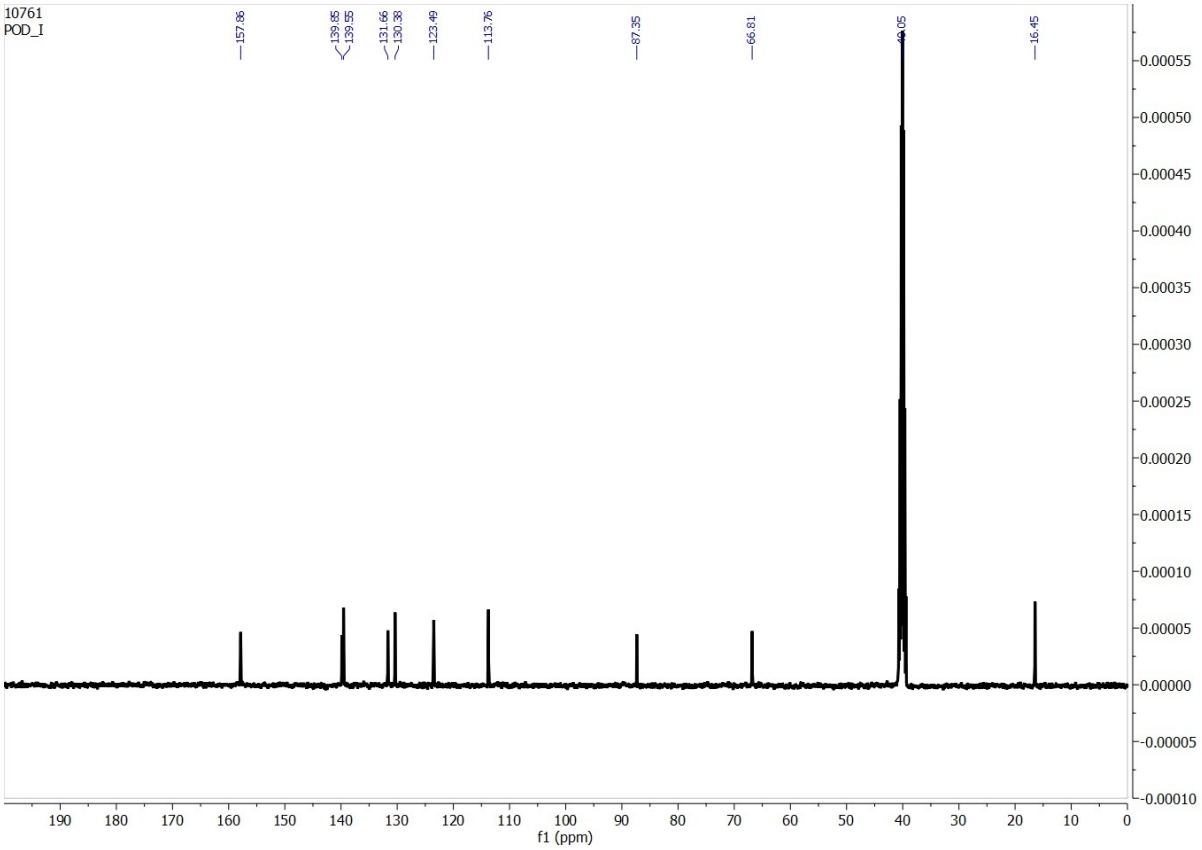

Fig. S7. ^{13}C-NMR spectrum of **P5** in DMSO-D_6.

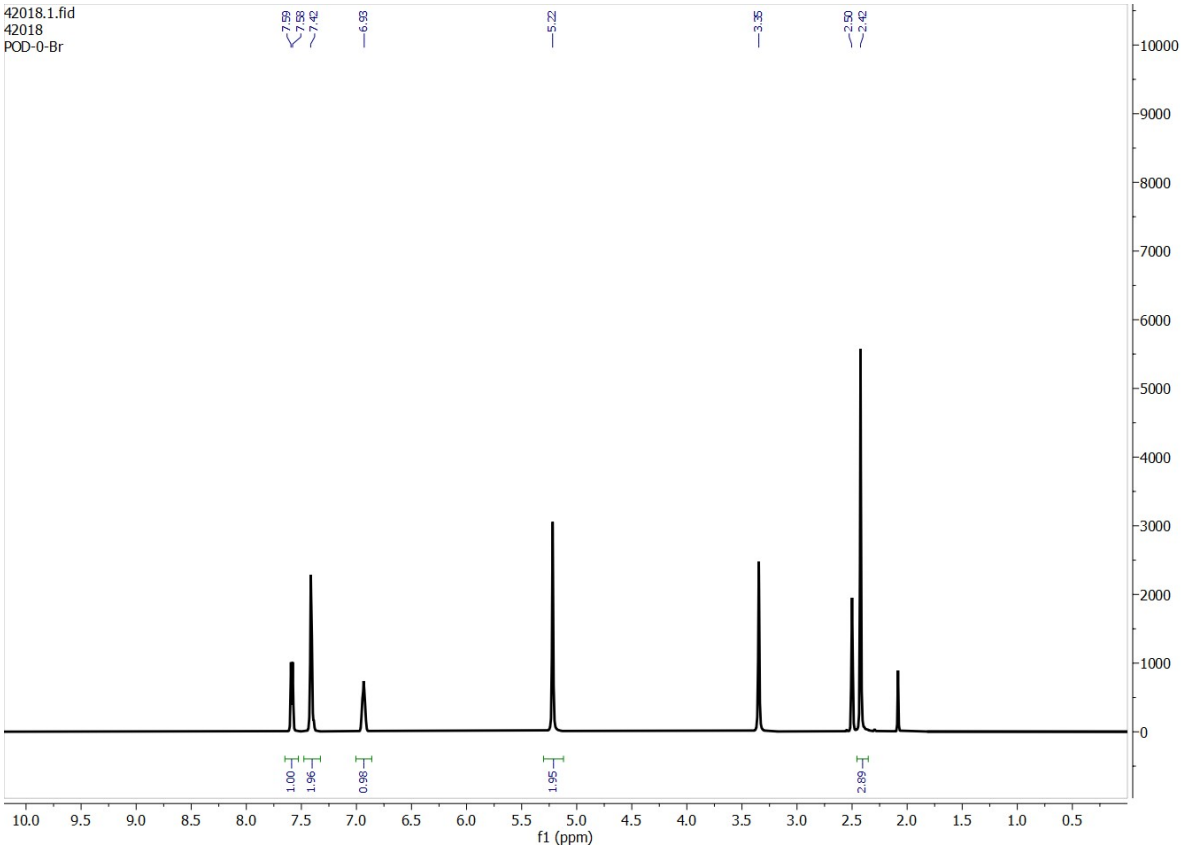

Fig. S8. ^{1}H-NMR spectrum of **P6** in DMSO-D_6.

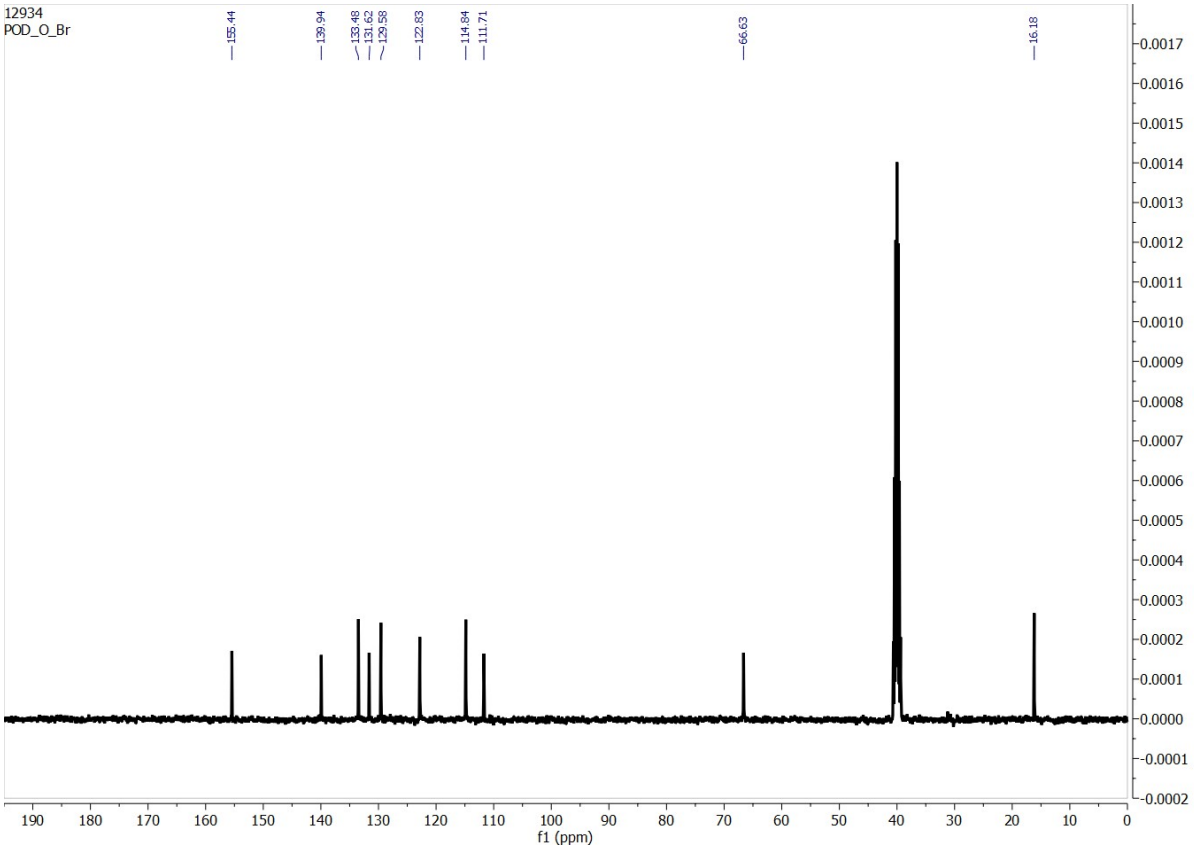

Fig. S9. ^{13}C-NMR spectrum of **P6** in DMSO-D_6.

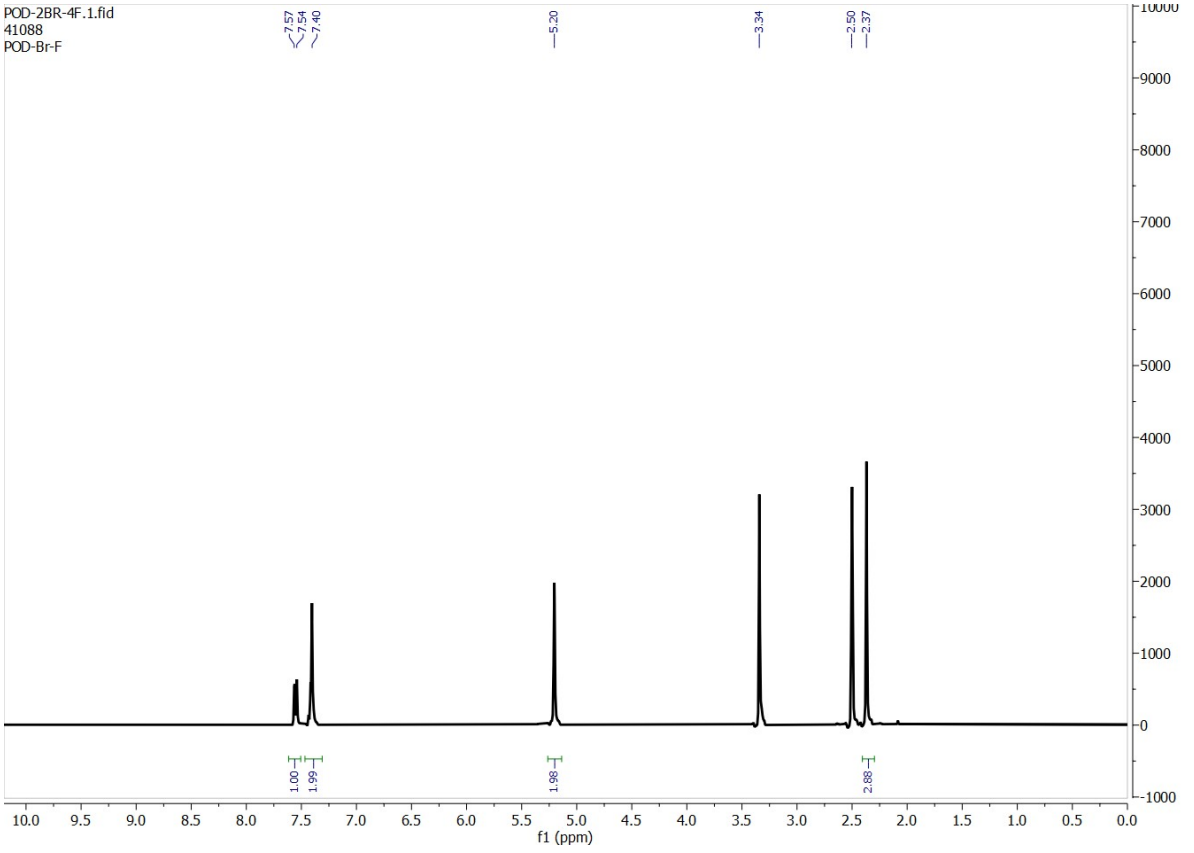

Fig. S10. ^{1}H-NMR spectrum of **P7** in DMSO-D_6.

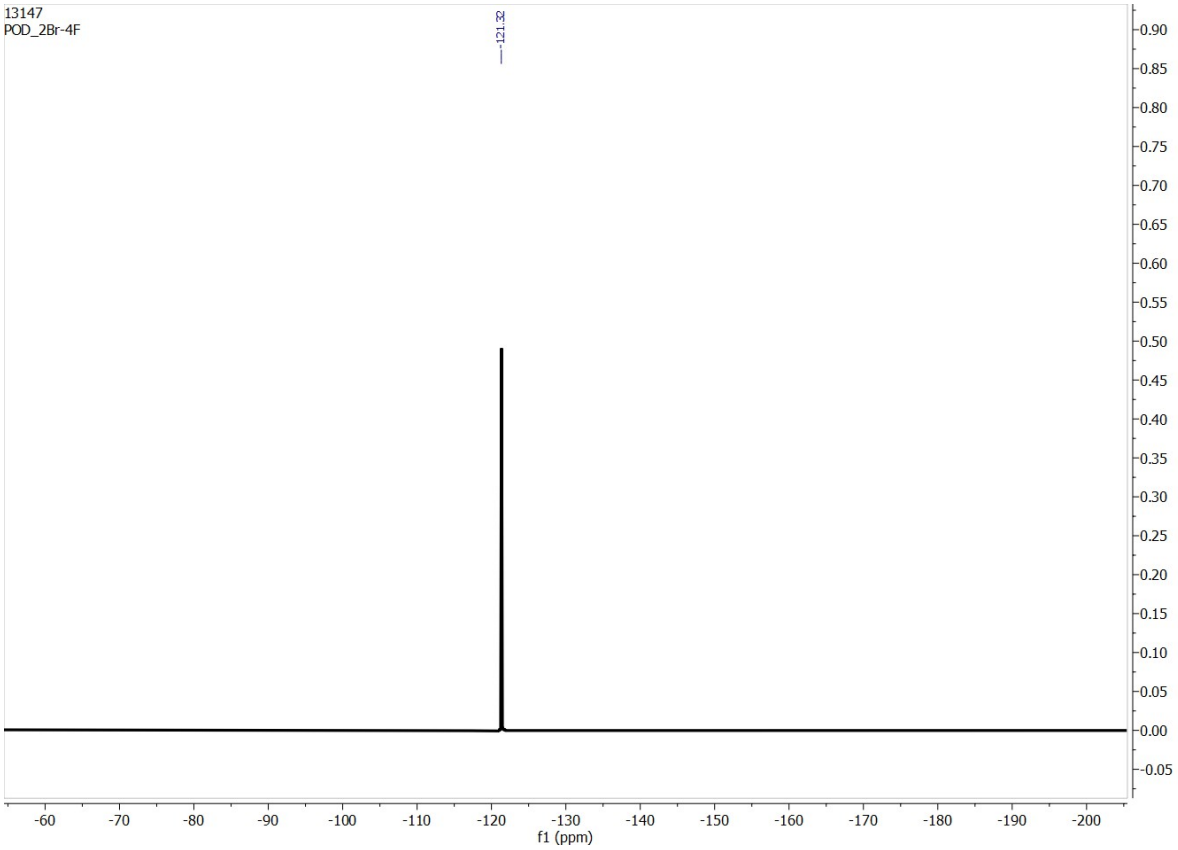

Fig. S11. ^{19}F-NMR spectrum of **P7** in DMSO-D_6.

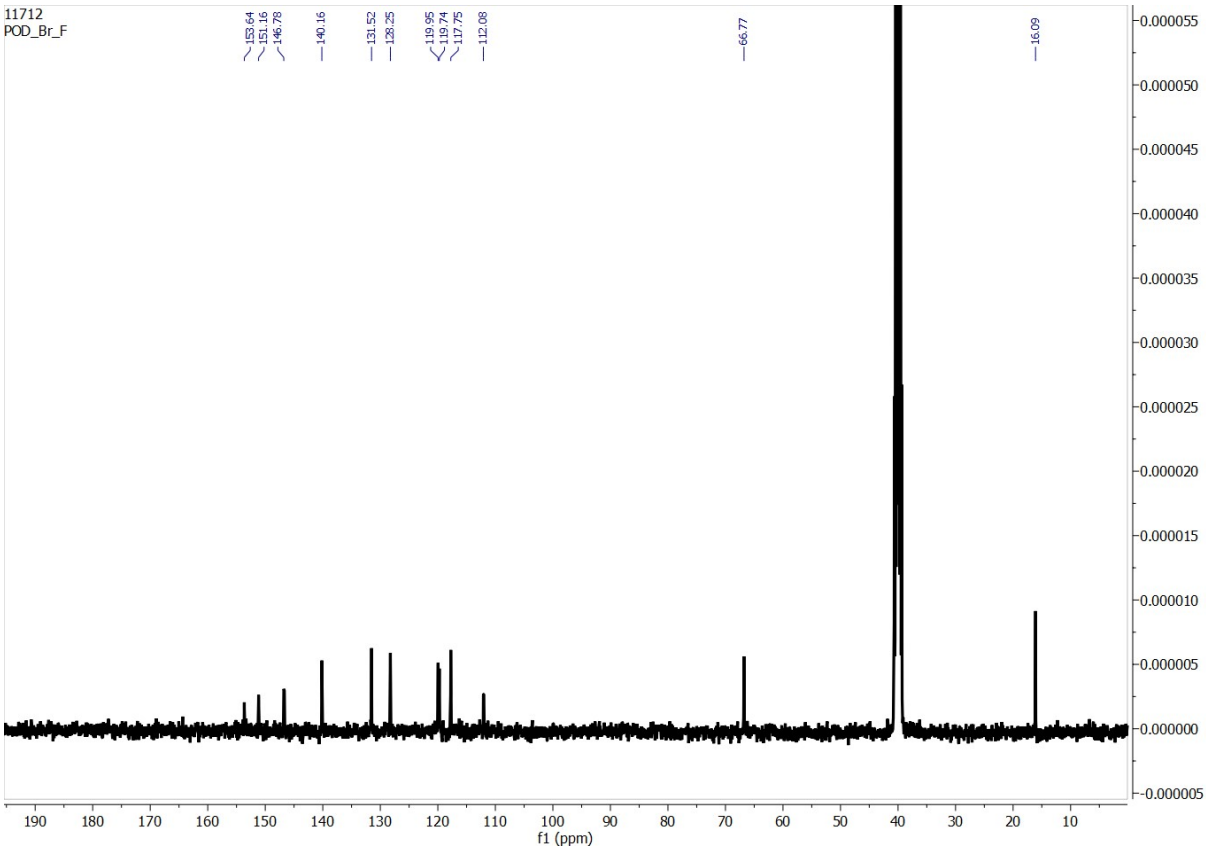

Fig. S12. ^{13}C-NMR spectrum of **P7** in DMSO-D_6.

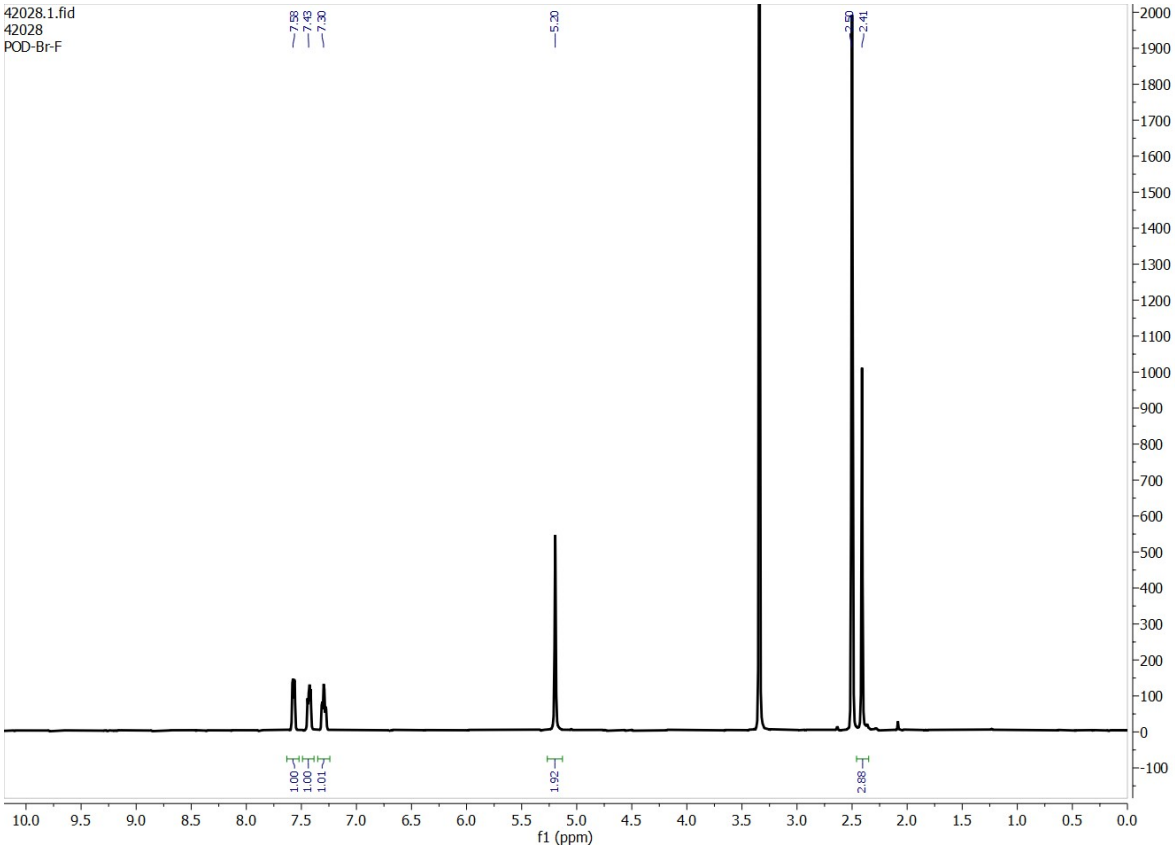

Fig. S13. ^{1}H-NMR spectrum of **P8** in DMSO-D_6.

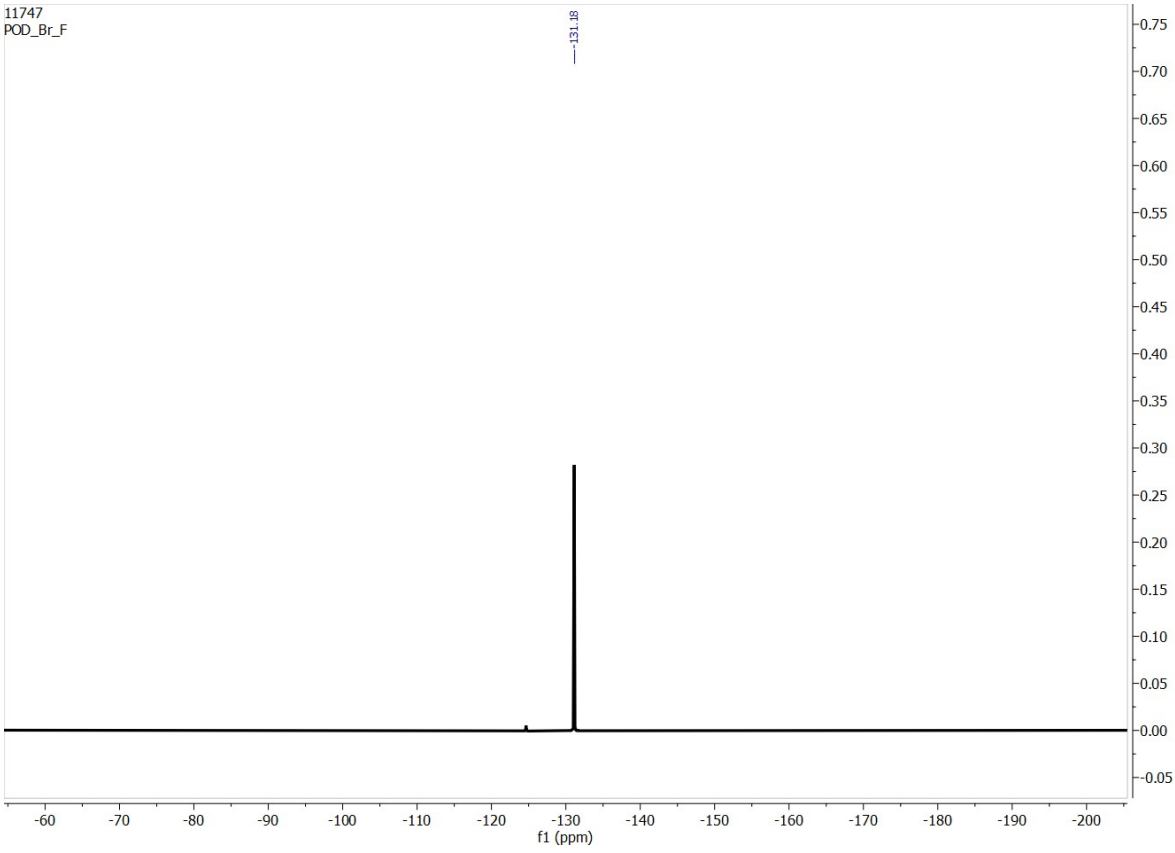

Fig. S14. ^{19}F-NMR spectrum of **P8** in DMSO-D_6.

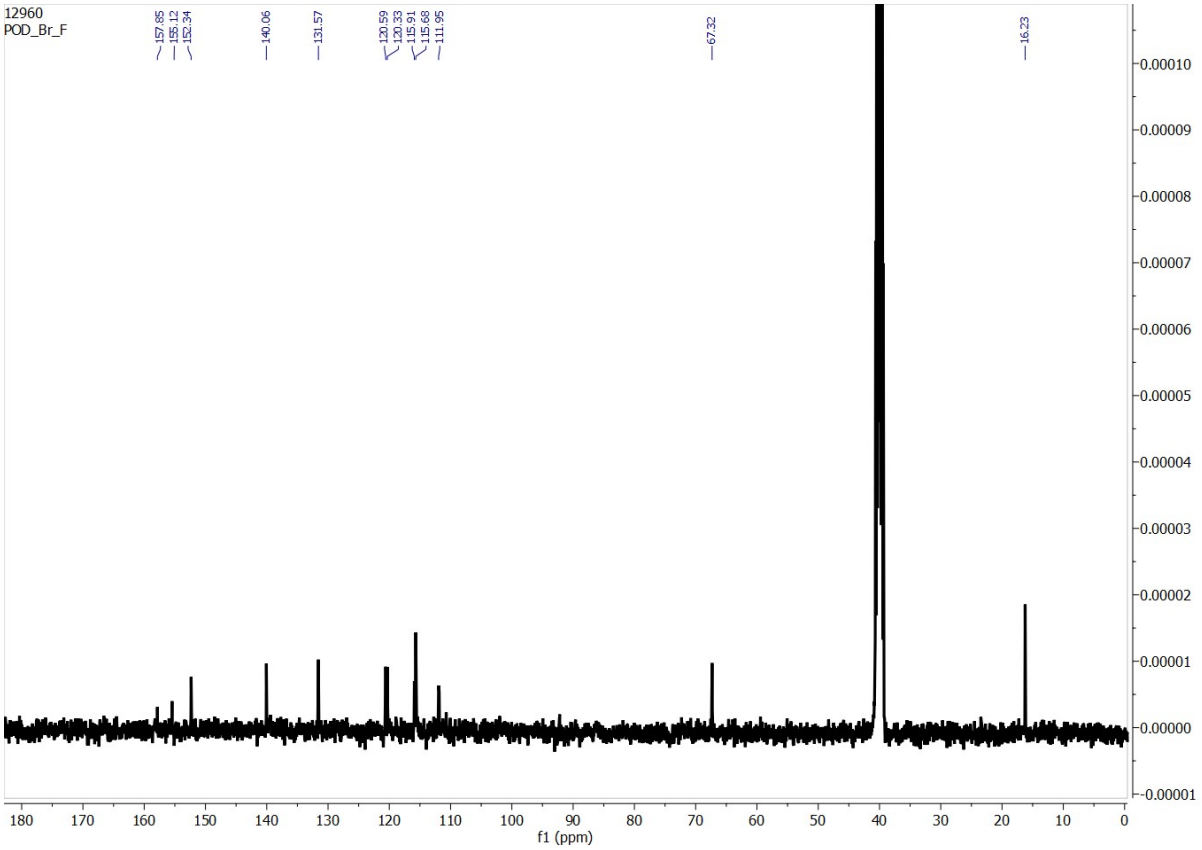

Fig. S15. ^{13}C-NMR spectrum of **P8** in DMSO-D_6.

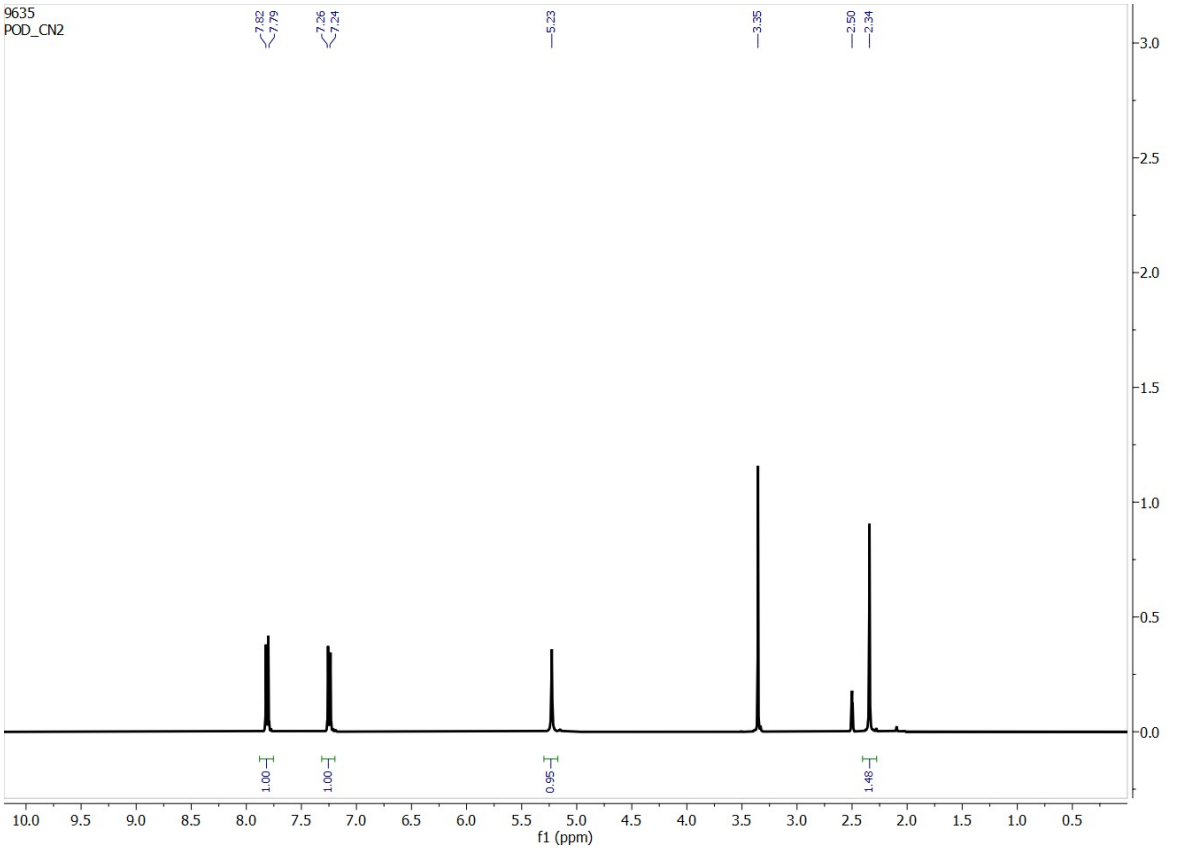

Fig. S16. ^{1}H-NMR spectrum of **P9** in DMSO-D_6.

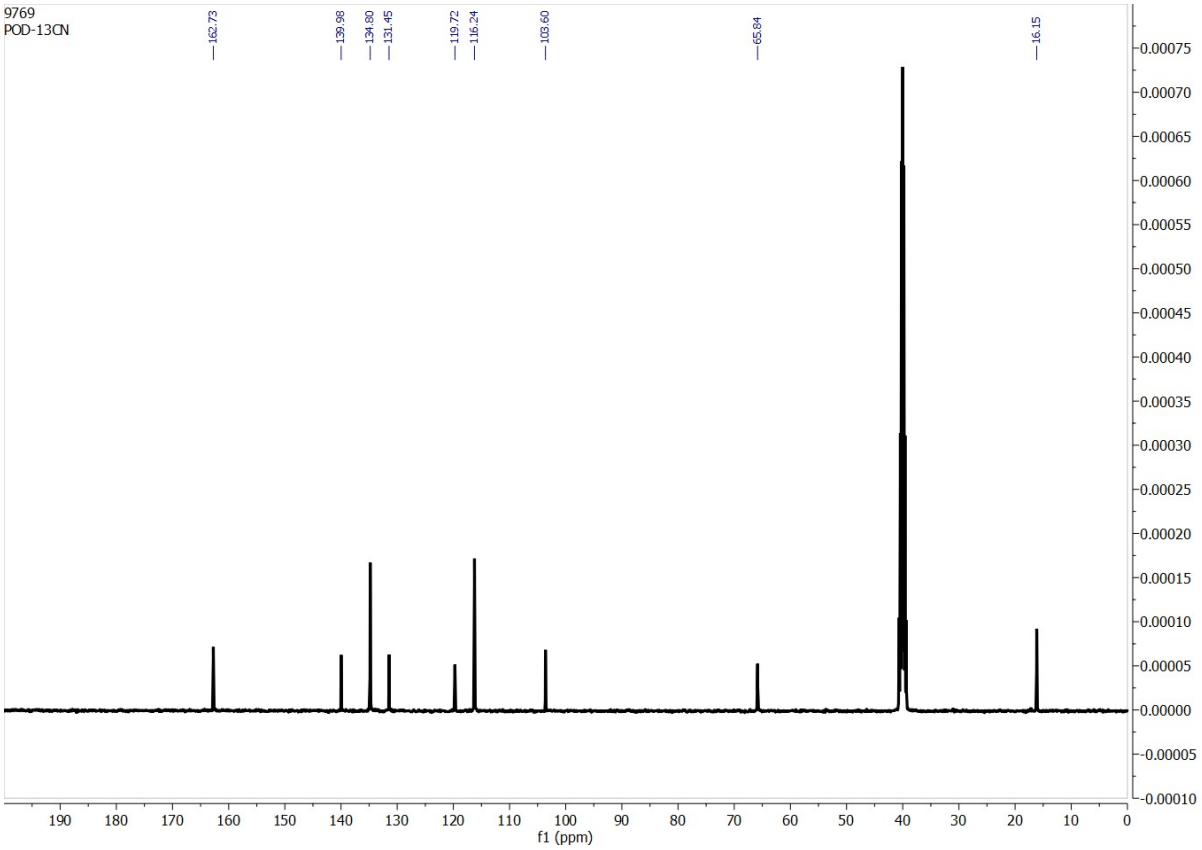

Fig. S17. ^{13}C-NMR spectrum of **P9** in DMSO-D_6.

3. X-ray diffraction studies of podand crystals

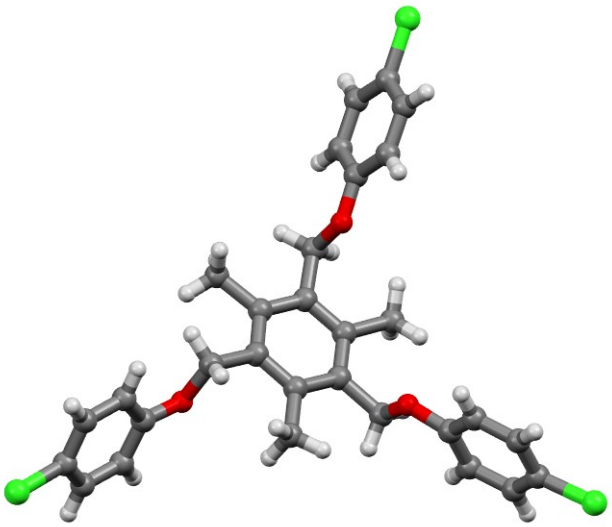

Fig. S18. Asymmetric unit of the single crystal X-ray structure of **P2**.

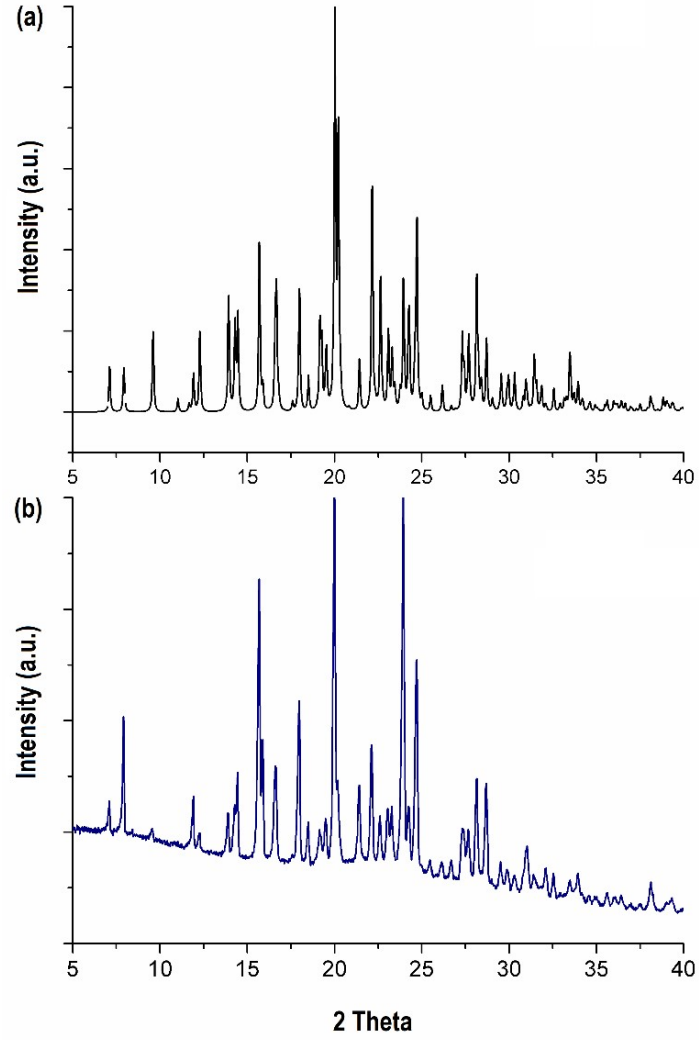

Fig. S19. (a) Simulated powder X-ray diffraction patterns of **P2**, and (b) experimental powder X-ray diffraction patterns of the bulk crystals of **P2** after drying.

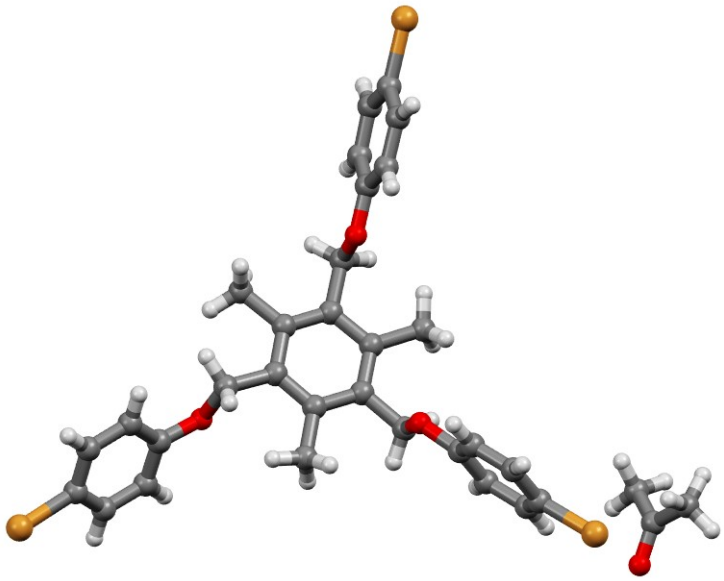

Fig. S20. Asymmetric unit of the single crystal X-ray structure of [**P3**·$(CH_3)_2CO$].

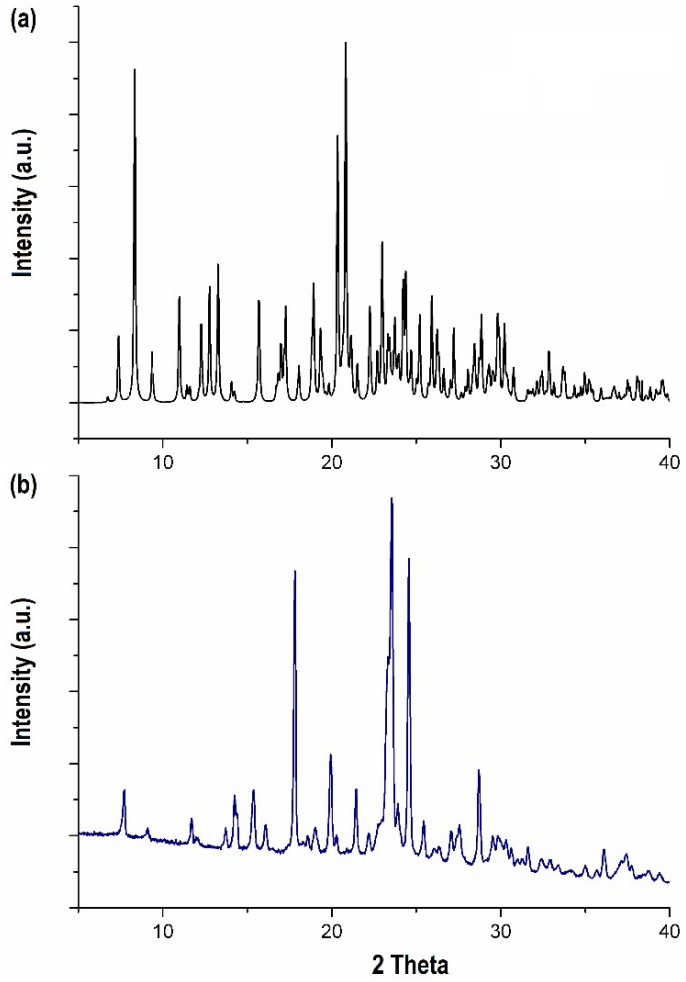

Fig. S21. (a) Simulated powder X-ray diffraction patterns of [**P3**·$(CH_3)_2CO$], and (b) experimental powder X-ray diffraction patterns of the bulk crystals of [**P3**·$(CH_3)_2CO$] after drying.

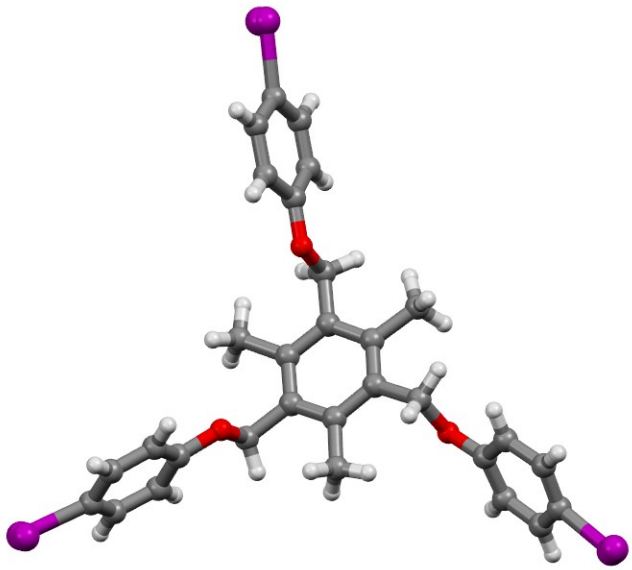

Fig. S22. Asymmetric unit of the single crystal X-ray structure of [**P4**·solvent].

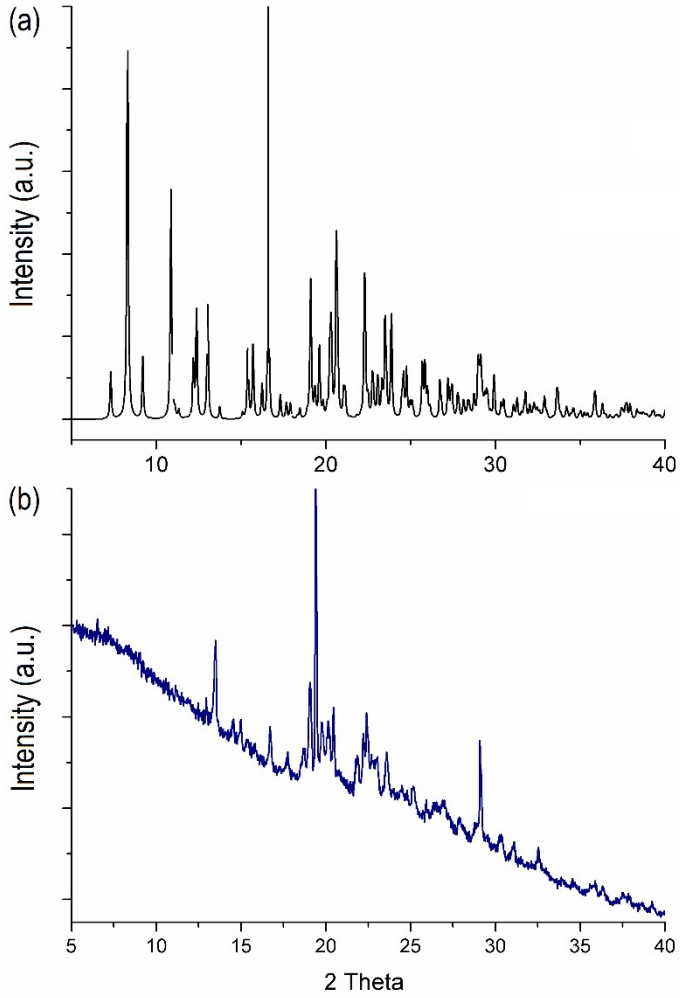

Fig. S23. (a) Simulated powder X-ray diffraction patterns of [**P4**·solvent], and (b) experimental powder X-ray diffraction patterns of [**P4**·solvent] after drying.

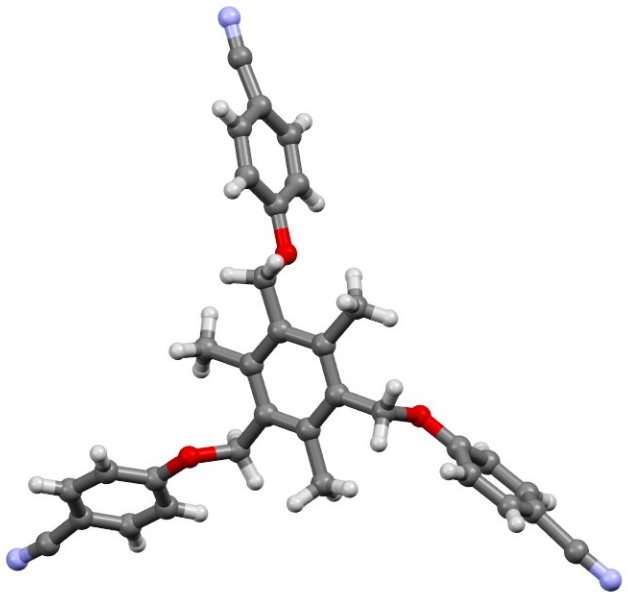

Fig. S24. Asymmetric unit of the single crystal X-ray structure of [**P9**·solvent].

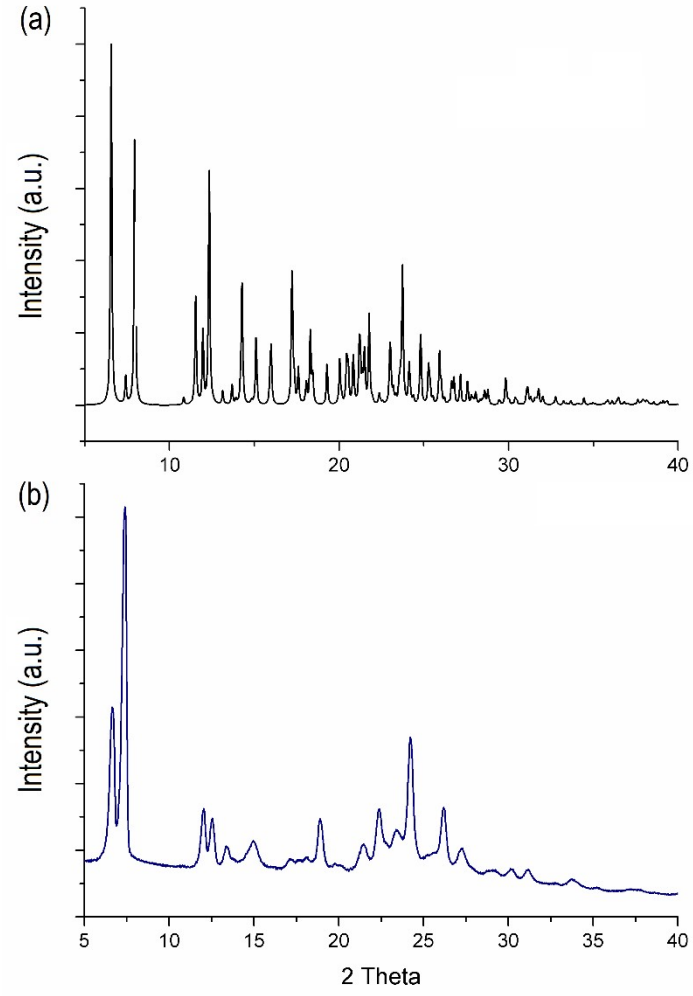

Fig. S25. (a) Simulated powder X-ray diffraction patterns of [**P9**·solvent], and (b) experimental powder X-ray diffraction patterns of [**P9**·solvent] after drying.

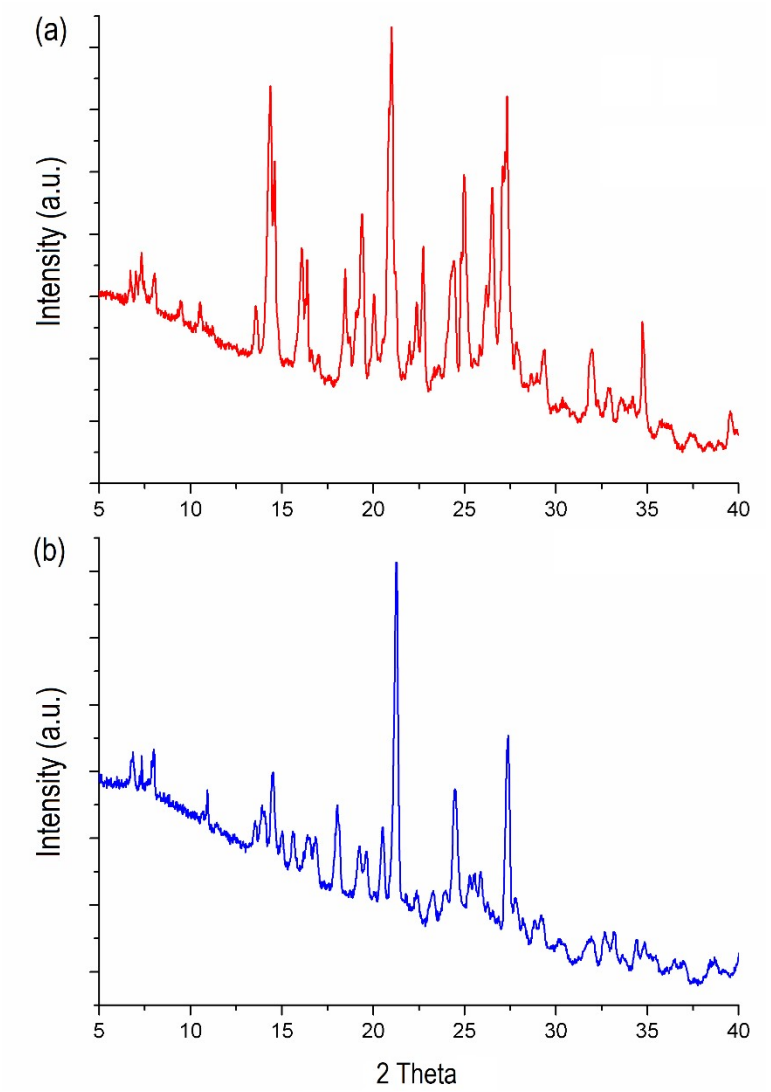

Fig. S26. (a) Experimental powder X-ray diffraction patterns of **P5** crystals obtained from acetone, (b) experimental powder X-ray diffraction patterns of **P6** crystals obtained from acetone.

Table S1. C-H hydrogen bond parameters observed in the crystal structures of ethereal podands.

Podands	C-H···A (A = acceptor)	C···A (Å)	H···A (Å)	<C-H···A (°)
P2	C22-H22B···O2	3.506(3)	2.66	145
	C28-H···O2	3.679(3)	2.78	161
	C22-H22A···π (mesitylene)	3.550	2.81	133
	C3-H3···π (PhCl3)	3.581	2.71	155
	C15-H15···π (mesitylene)	3.495	2.58	166
	C30-H30B···π (PhCl3)	4.130	3.20	162
[**P3**·$(CH_3)_2CO$]	C24-H24B···O1	3.587(1)	2.70	150
	C26-H26···O1	3.721(1)	2.81	165
	C24-H24A···π (mesitylene)	3.539	2.86	127
	C19-H19···π (PhBr3)	3.659	2.84	146
	C2-H2···π (mesitylene)	3.554	2.67	158
	C13-H13C···π (PhBr3)	3.681	2.87	141
	C23-H23···Br3	3.855	3.11	138
[**P4**·solvent]	C10-H10A···O2	3.572(1)	2.69	151
	C12-H12···O2	3.716(1)	2.82	161
	C10-H10A···π (mesitylene)	3.530	2.86	127
	C30-H30···π (PhI1)	3.684	2.85	149
	C20-H20···π (mesitylene)	3.711	2.84	156
	C8-H8A···π (PhI1)	4.015	3.31	131
	C26-H26···I1	3.881	3.12	140
[**P9**·solvent]	C14-H14C···O1	3.544(5)	2.65	153
	C17-H17A···N1	3.392(2)	2.43	175
	C28-H28···N2	3.602(2)	2.68	172
	C14-H14B···N3	3.555(2)	2.69	151
	C23-H23···C33 (-CN)	3.654(2)	2.85	145

4. Thermogravimetry analysis of crystals under nitrogen atmosphere

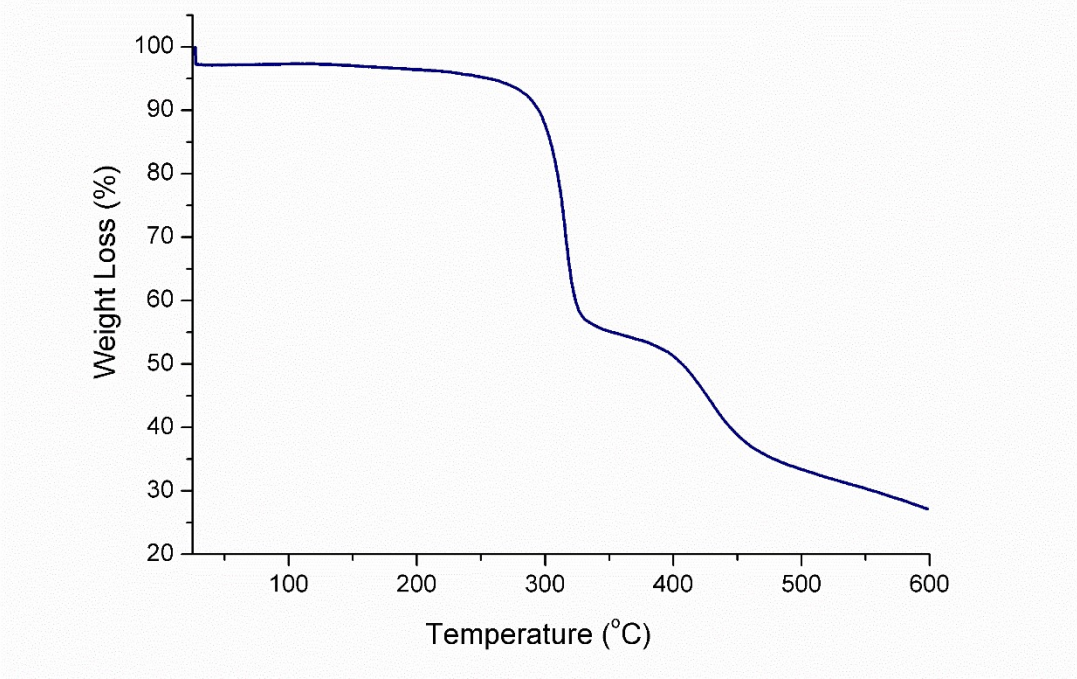

Fig. S27. Thermogravimetric analysis of the crystals of **P1** obtained from acetone.

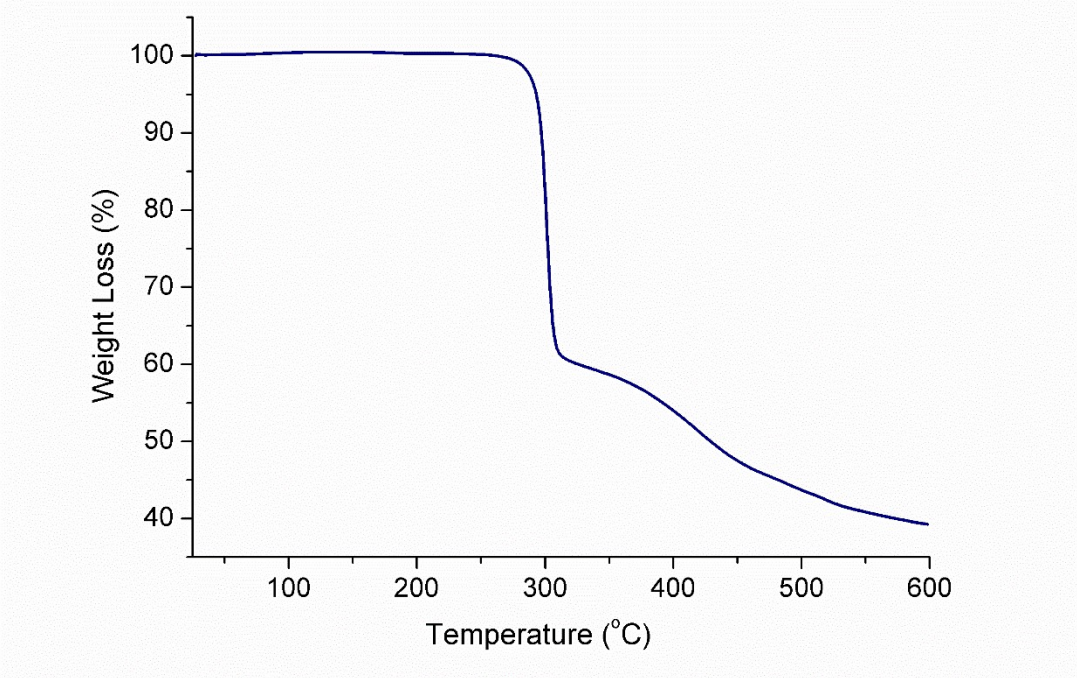

Fig. S28. Thermogravimetric analysis of the crystals of **P2** obtained from acetone-ethanol solvents (2:1, v/v).

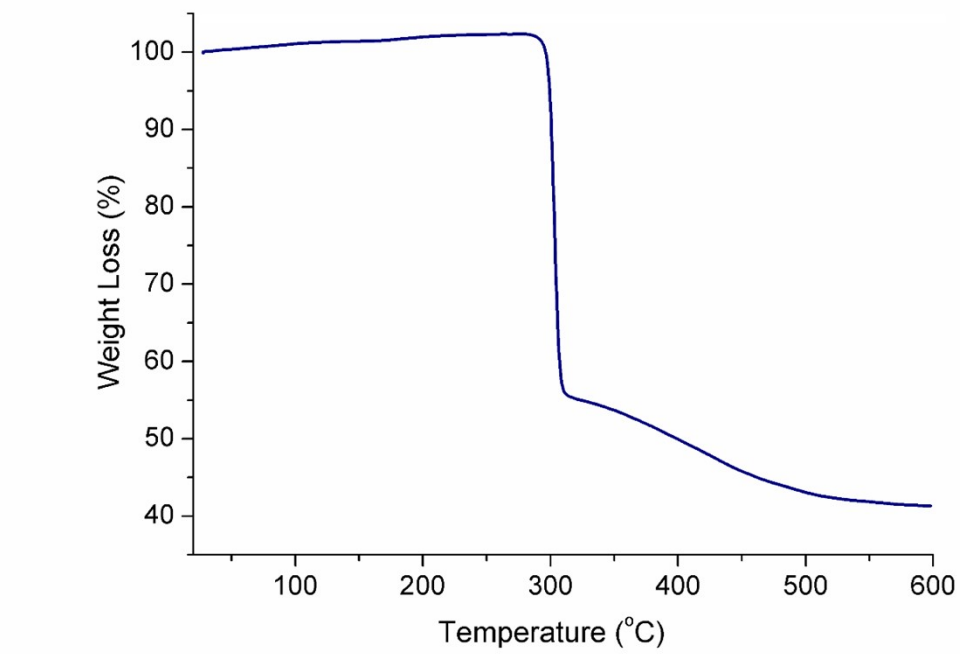

Fig. S29. Thermogravimetric analysis of the crystals of [**P3**·$(CH_3)_2CO$] obtained from acetone-ethanol (2:1, v/v).

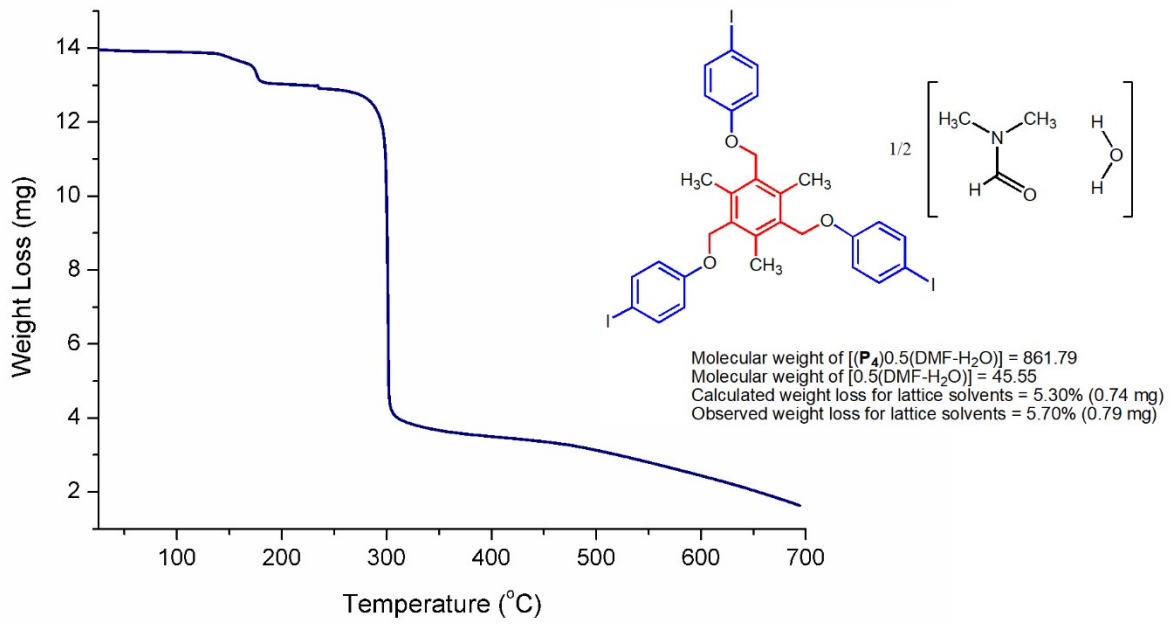

Fig. S30. Thermogravimetric analysis of the crystals of [**P4**·0.5(DMF-H_2O)] obtained from acetone-DMF (2:1, v/v).

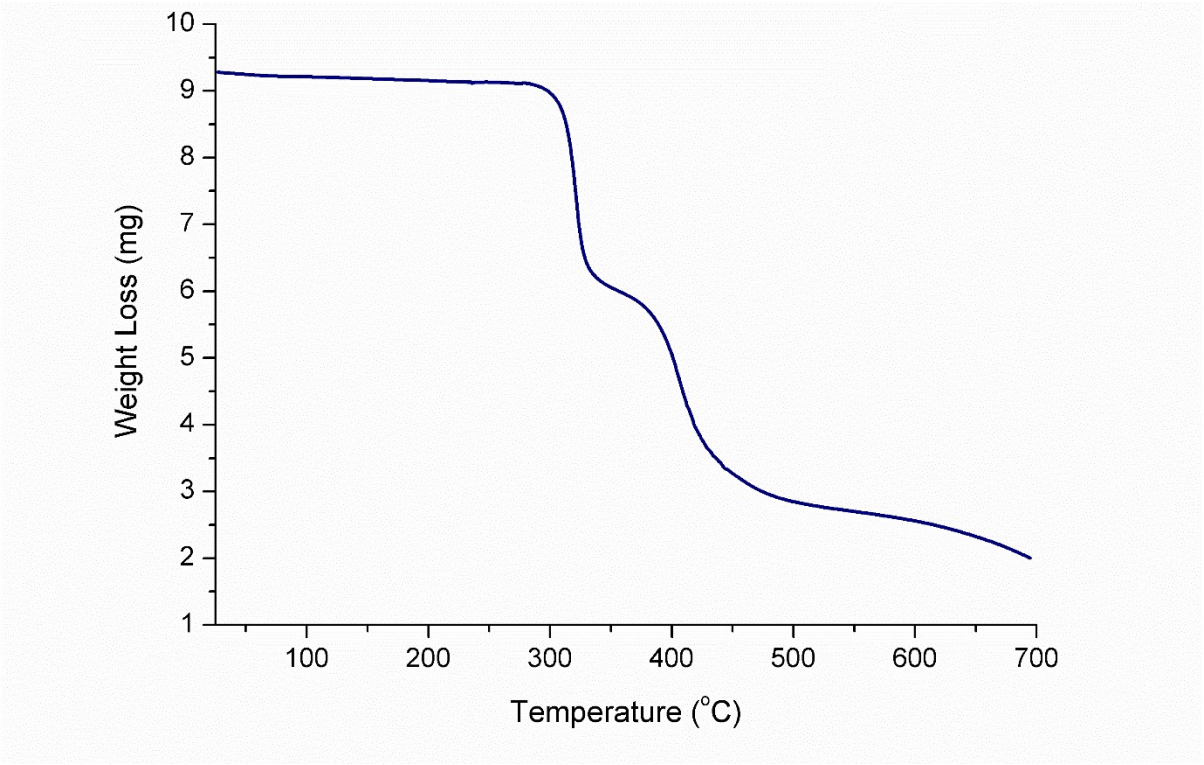

Fig. S31. Thermogravimetric analysis of the crystals of [**P9**·solvent] obtained from acetone-acetonitrile solution.

5. Hirshfeld surface analysis fingerprint plots

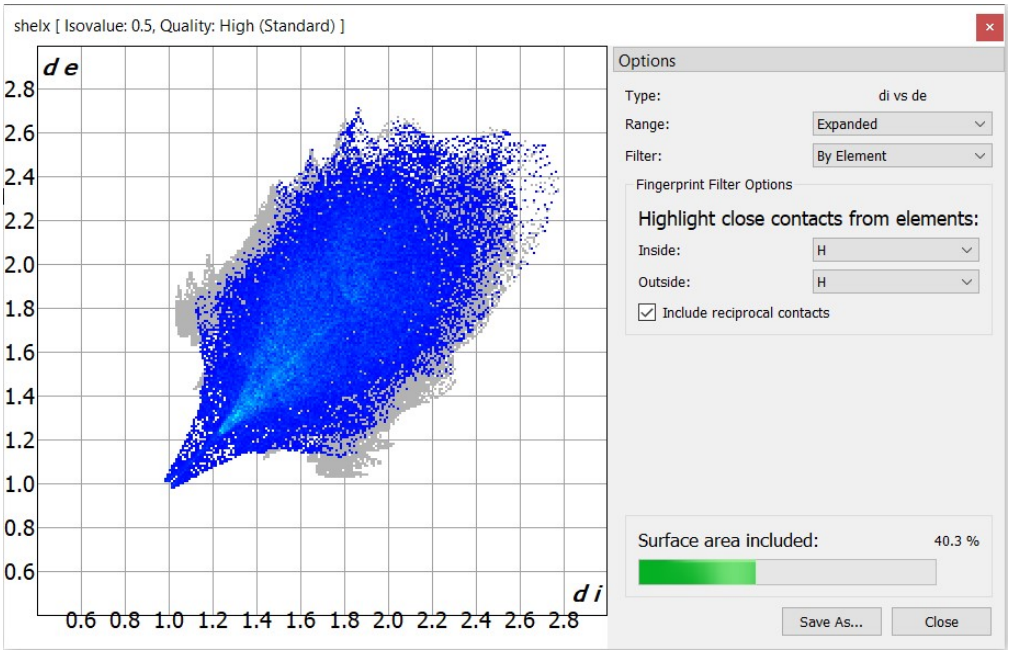

Fig. S32. Hirshfeld surface generated 2D fingerprint plot highlighting the relative contribution from H···H close contacts in the crystal structure of **P2**.

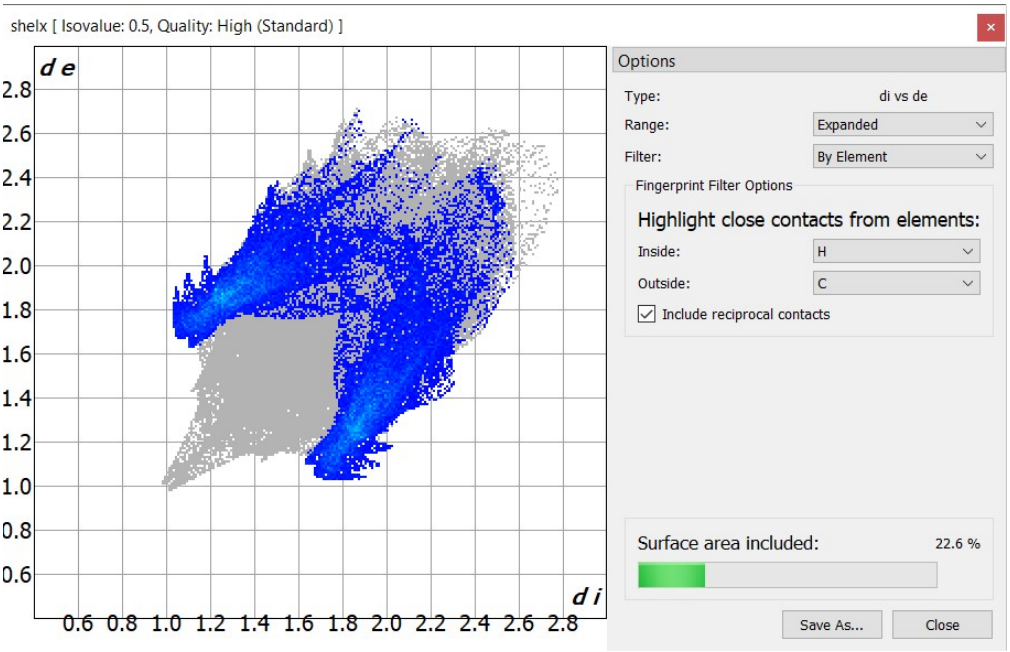

Fig. S33. Hirshfeld surface generated 2D fingerprint plot highlighting the relative contribution from H···C close contacts in the crystal structure of **P2**.

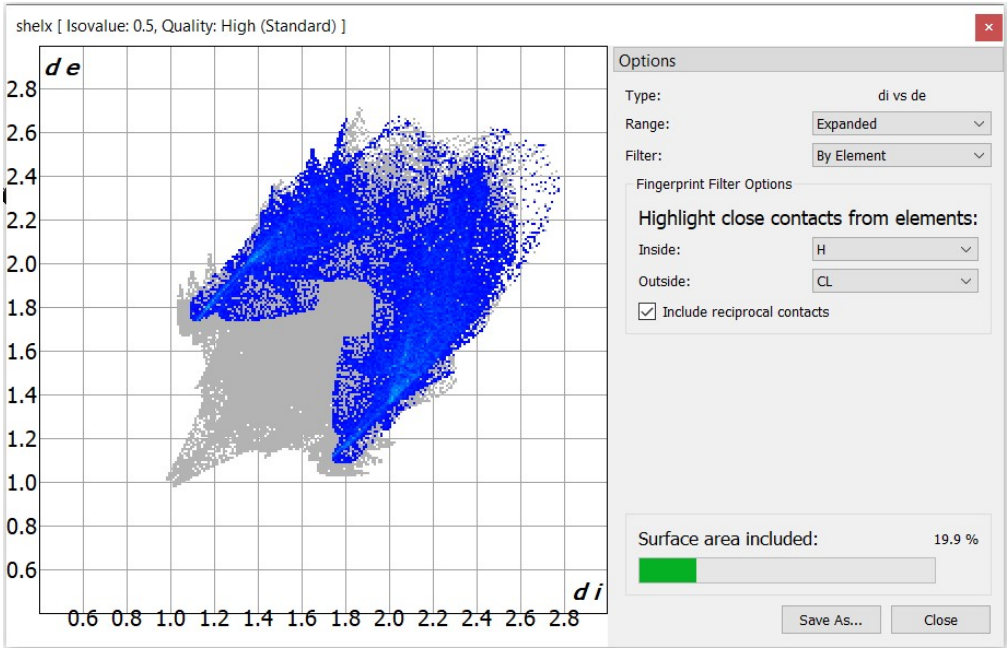

Fig. S34. Hirshfeld surface generated 2D fingerprint plot highlighting the relative contribution from H···Cl close contacts in the crystal structure of **P2**.

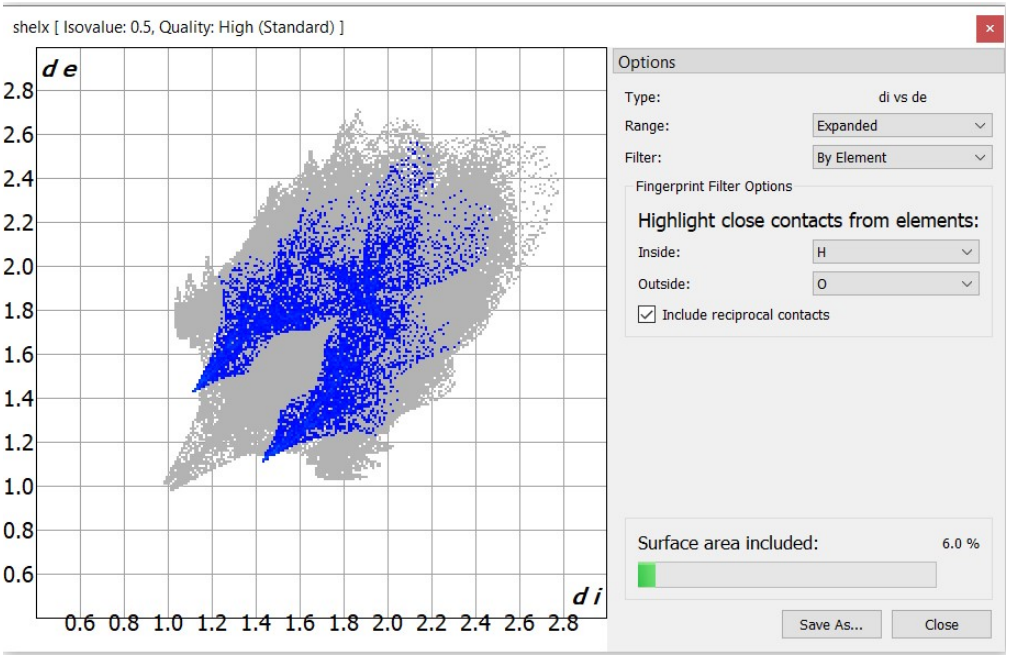

Fig. S35. Hirshfeld surface generated 2D fingerprint plot highlighting the relative contribution from H···O close contacts in the crystal structure of **P2**.

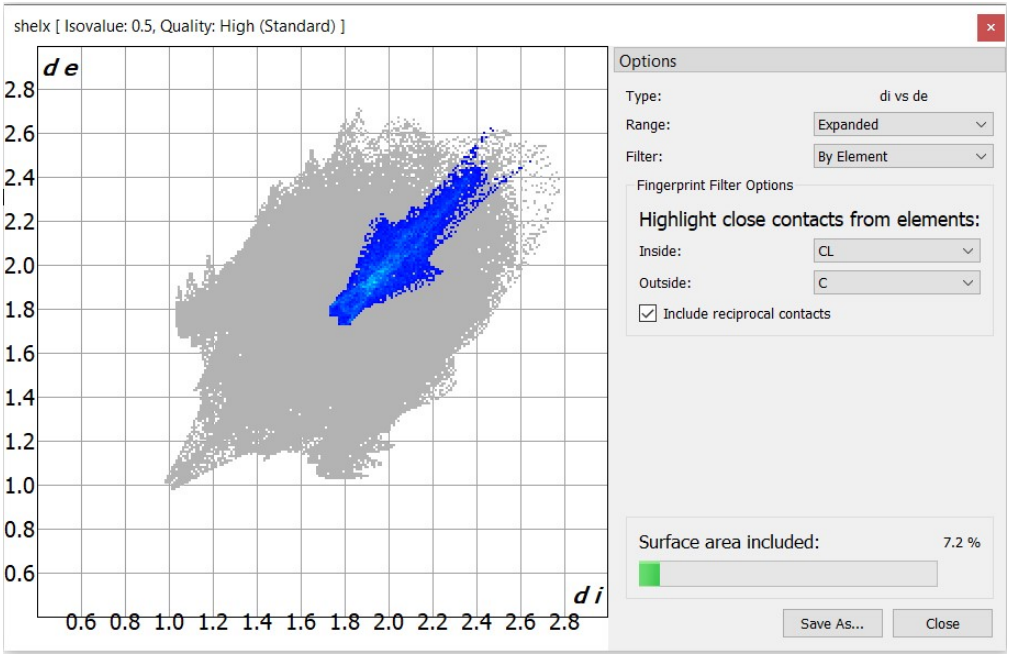

Fig. S36. Hirshfeld surface generated 2D fingerprint plot highlighting the relative contribution from Cl···C close contacts in the crystal structure of **P2**.

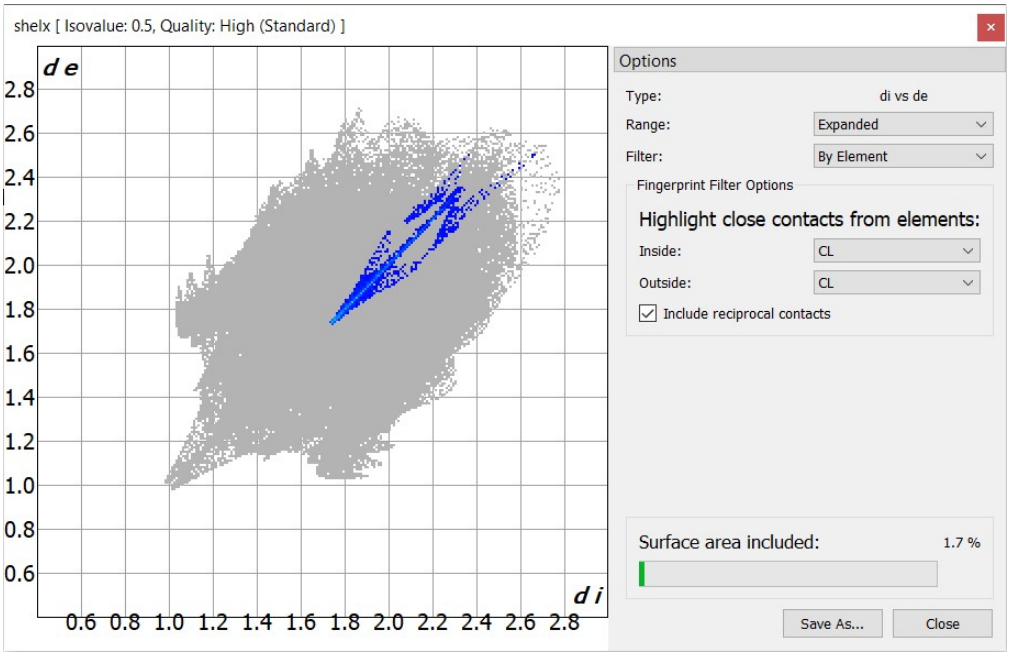

Fig. S37. Hirshfeld surface generated 2D fingerprint plot highlighting the relative contribution from Cl···Cl close contacts in the crystal structure of **P2**.

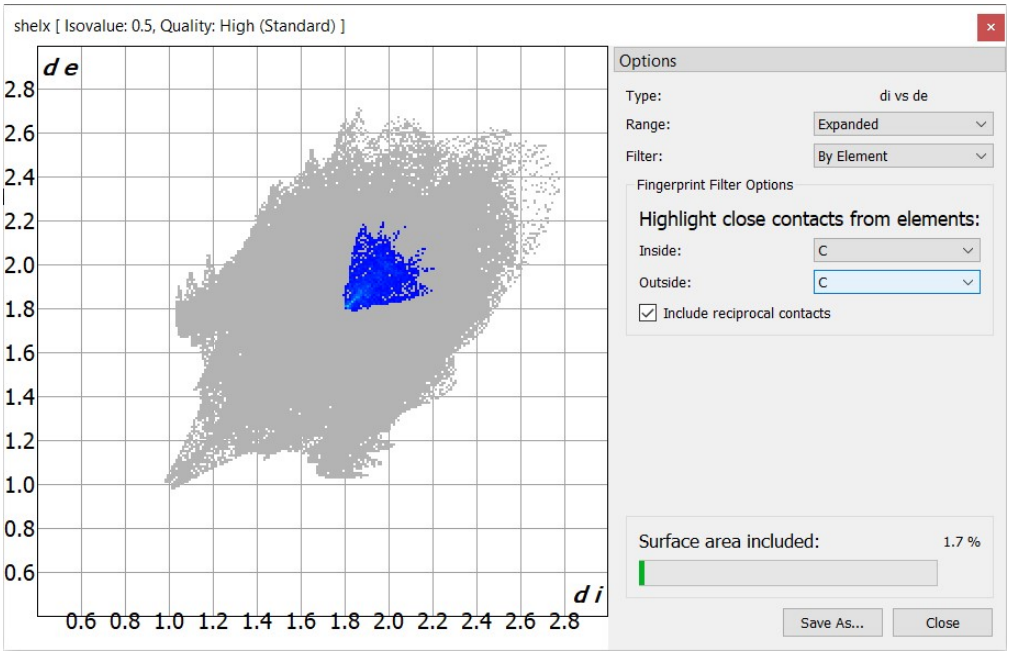

Fig. S38. Hirshfeld surface generated 2D fingerprint plot highlighting the relative contribution from C···C close contacts in the crystal structure of **P2**.

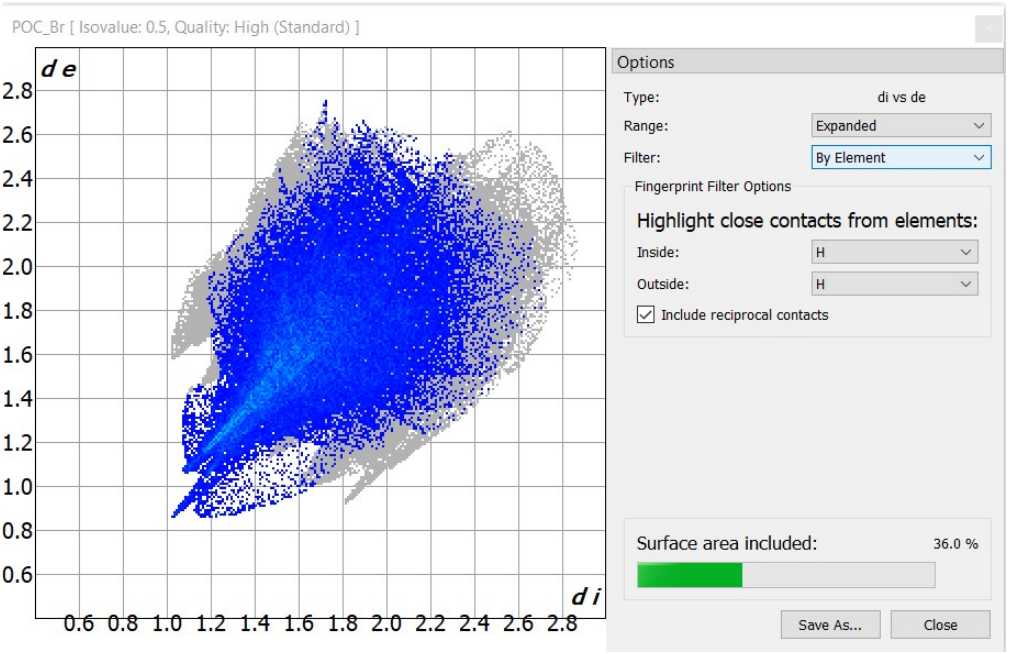

Fig. S39. Hirshfeld surface generated 2D fingerprint plot highlighting the relative contribution from H···H close contacts in the crystal structure of [**P3**·$(CH_3)_2CO$].

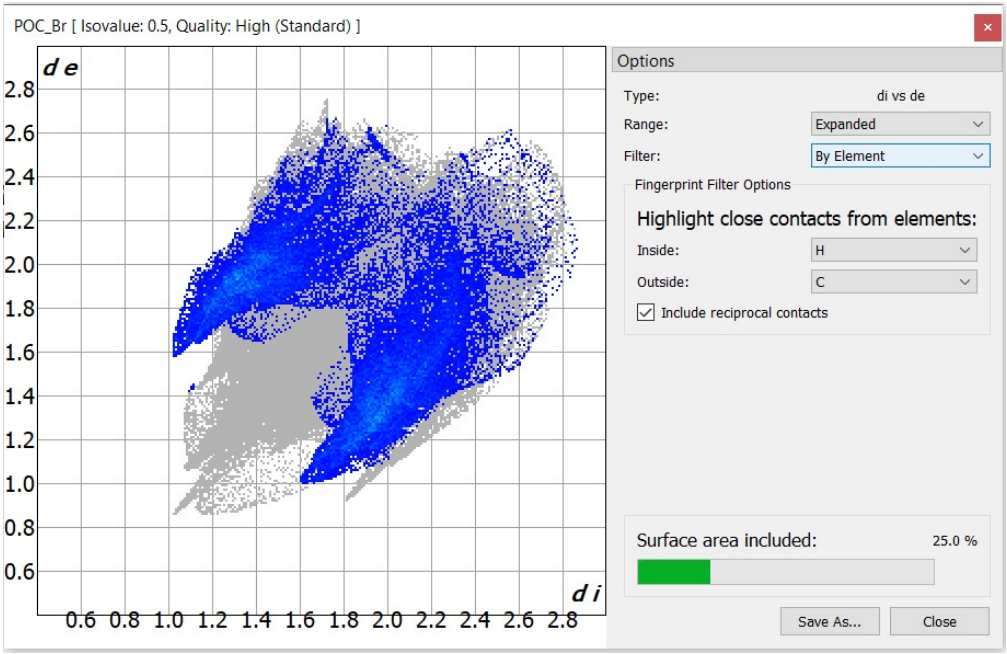

Fig. S40. Hirshfeld surface generated 2D fingerprint plot highlighting the relative contribution from H···C close contacts in the crystal structure of [**P3**·$(CH_3)_2CO$].

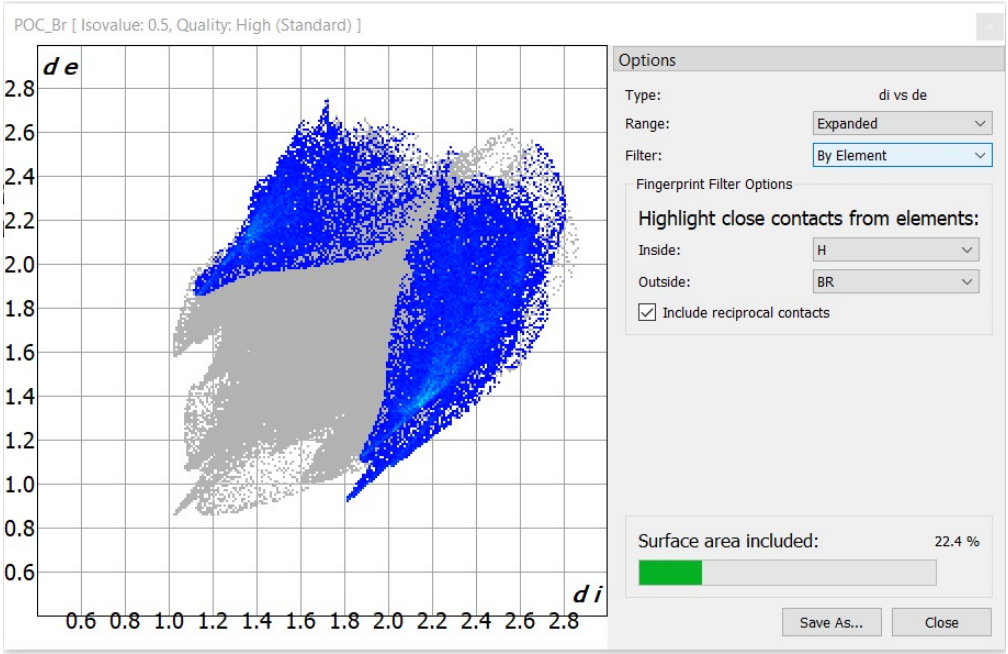

Fig. S41. Hirshfeld surface generated 2D fingerprint plot highlighting the relative contribution from H···Br close contacts in the crystal structure of [**P3**·$(CH_3)_2CO$].

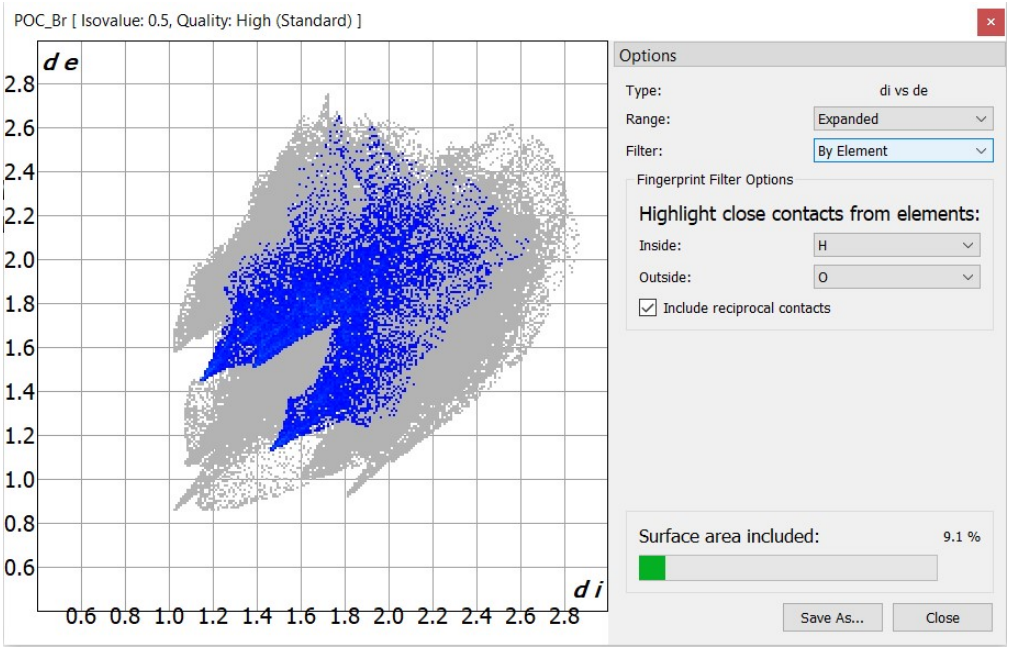

Fig. S42. Hirshfeld surface generated 2D fingerprint plot highlighting the relative contribution from H···O close contacts in the crystal structure of [**P3**·$(CH_3)_2CO$].

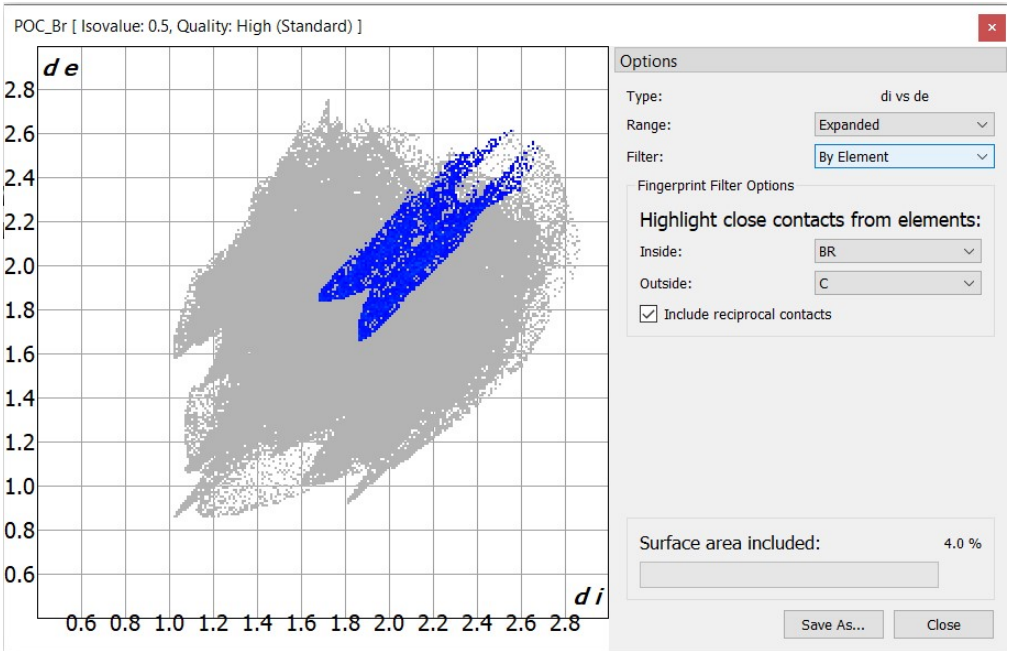

Fig. S43. Hirshfeld surface generated 2D fingerprint plot highlighting the relative contribution from Br···C close contacts in the crystal structure of [**P3**·$(CH_3)_2CO$].

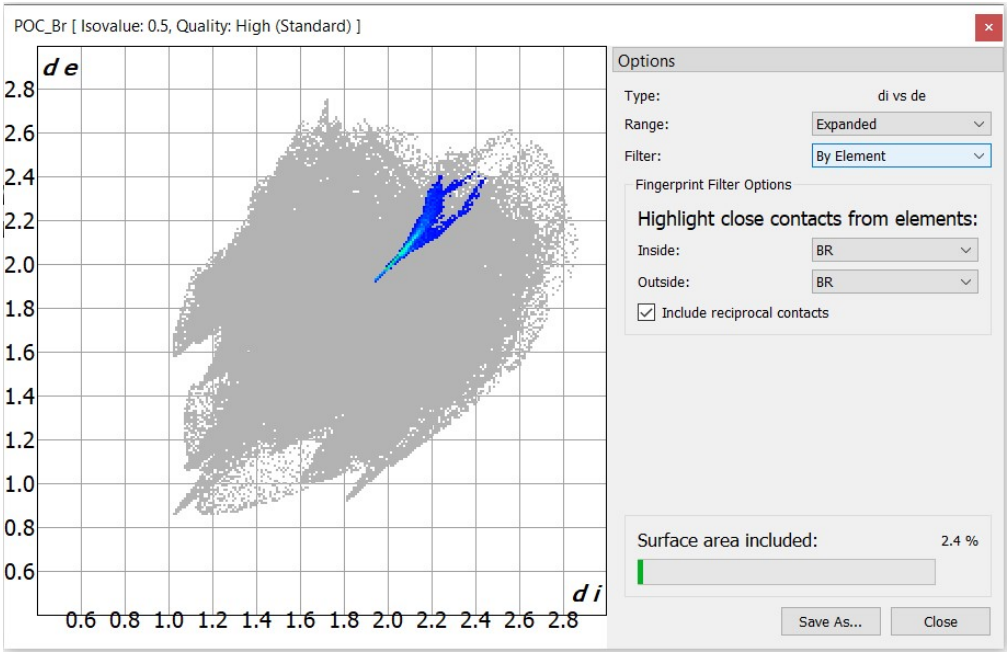

Fig. S44. Hirshfeld surface generated 2D fingerprint plot highlighting the relative contribution from Br···Br close contacts in the crystal structure of [**P3**·$(CH_3)_2CO$].

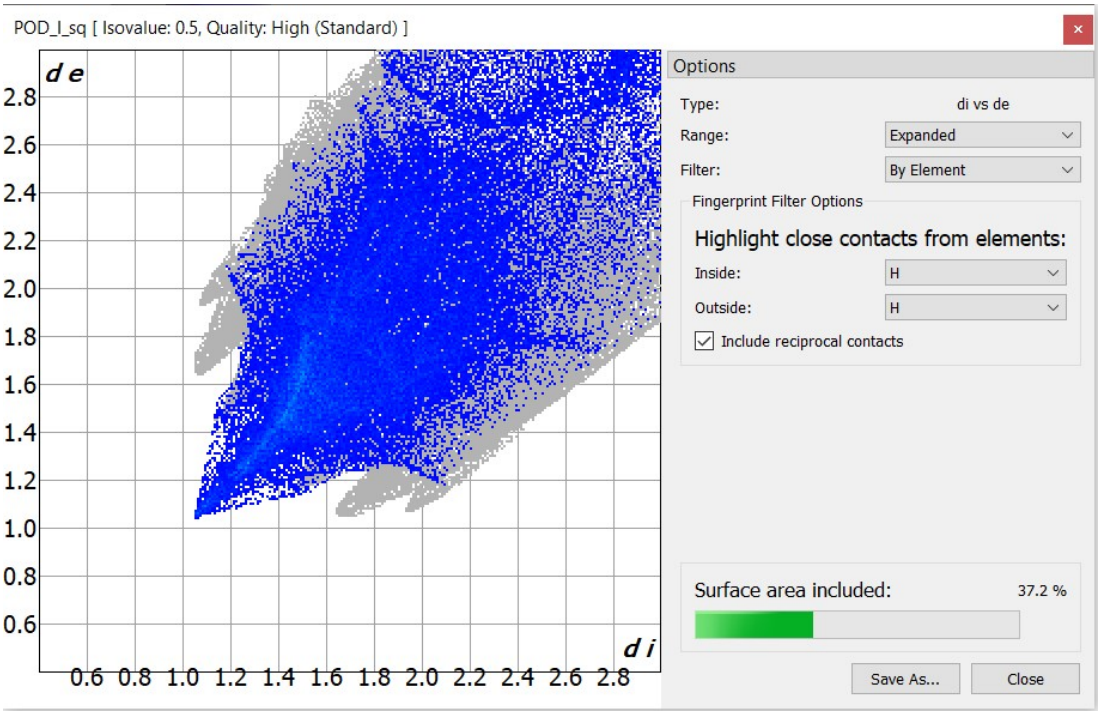

Fig. S45. Hirshfeld surface generated 2D fingerprint plot highlighting the relative contribution from H···H close contacts in the crystal structure of **P4**.

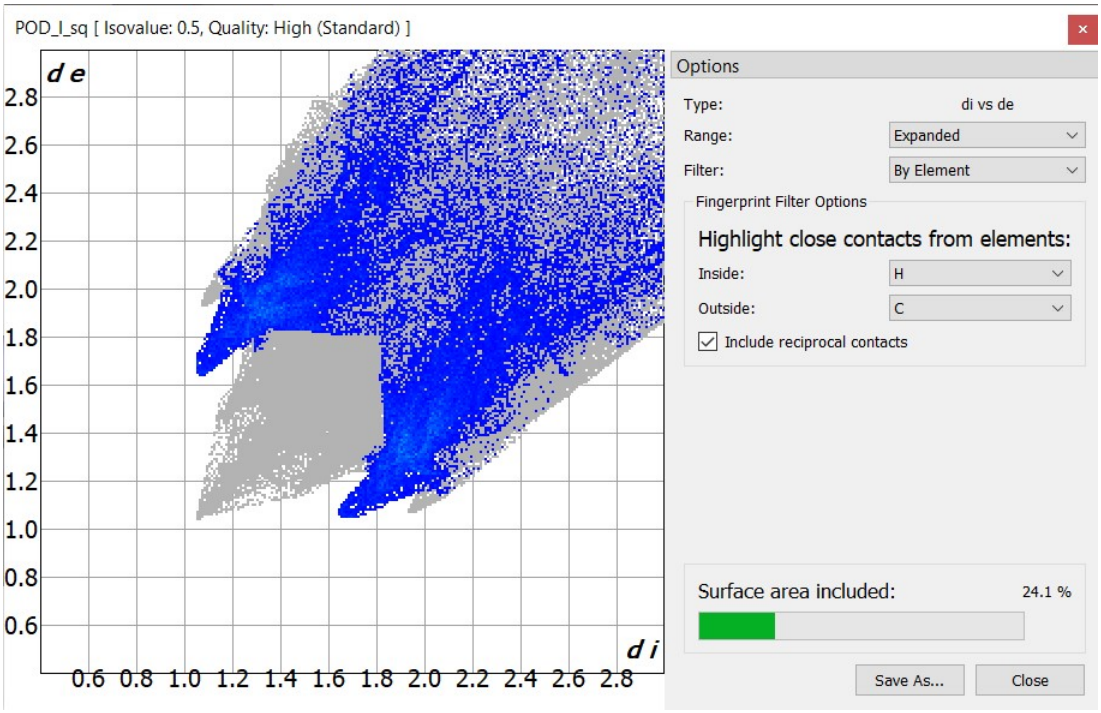

Fig. S46. Hirshfeld surface generated 2D fingerprint plot highlighting the relative contribution from H···C close contacts in the crystal structure of **P4**.

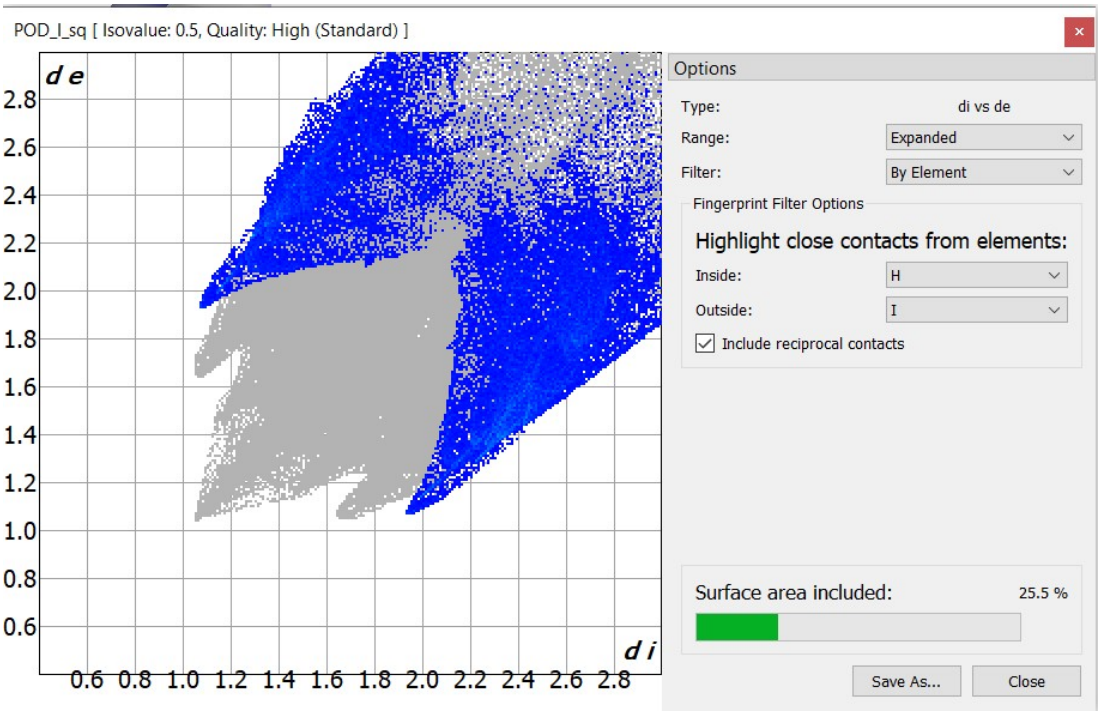

Fig. S47. Hirshfeld surface generated 2D fingerprint plot highlighting the relative contribution from H···I close contacts in the crystal structure of **P4**.

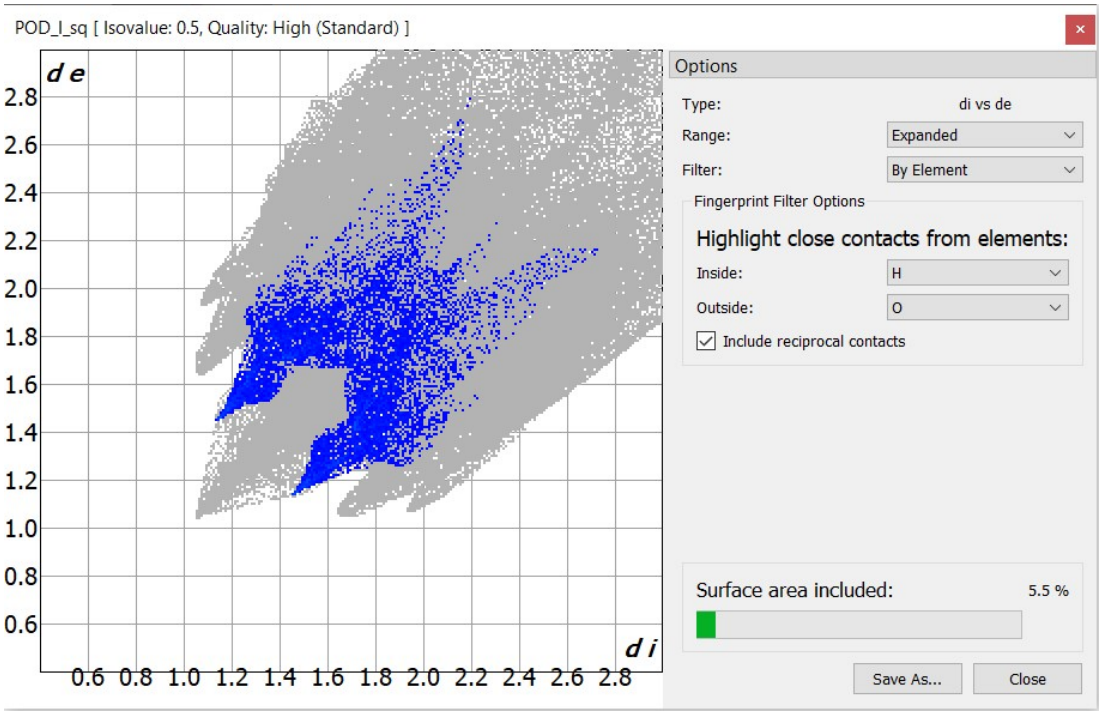

Fig. S48. Hirshfeld surface generated 2D fingerprint plot highlighting the relative contribution from H···O close contacts in the crystal structure of **P4**.

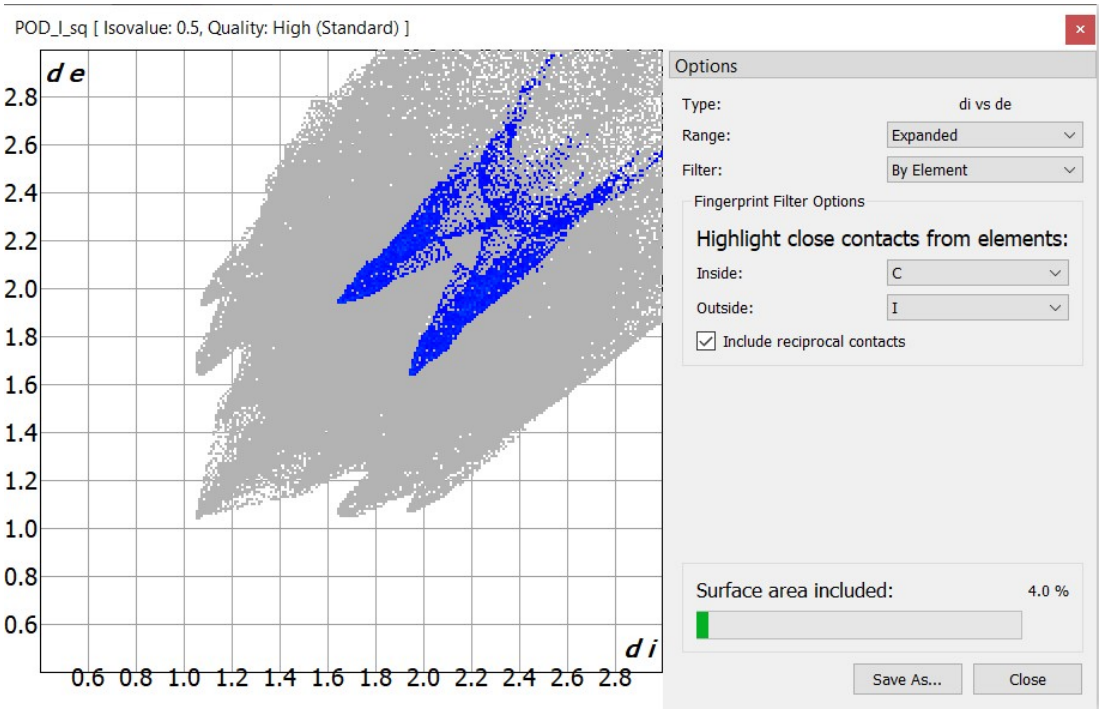

Fig. S49. Hirshfeld surface generated 2D fingerprint plot highlighting the relative contribution from C···I close contacts in the crystal structure of **P4**.

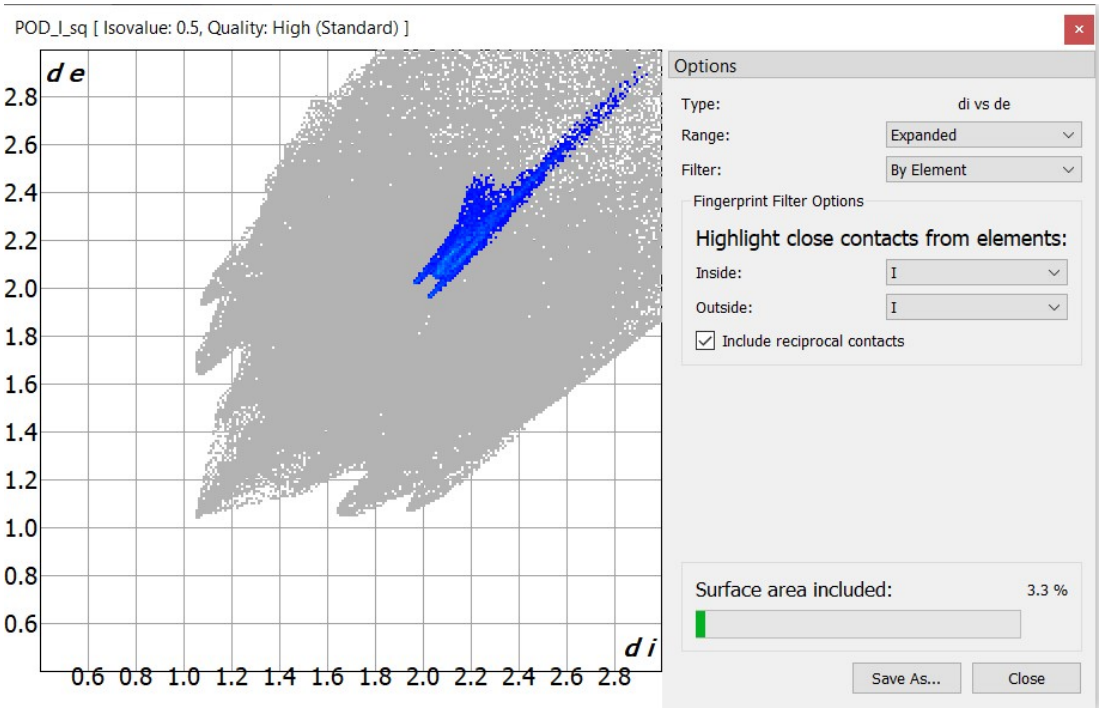

Fig. S50. Hirshfeld surface generated 2D fingerprint plot highlighting the relative contribution from I···I close contacts in the crystal structure of **P4**.

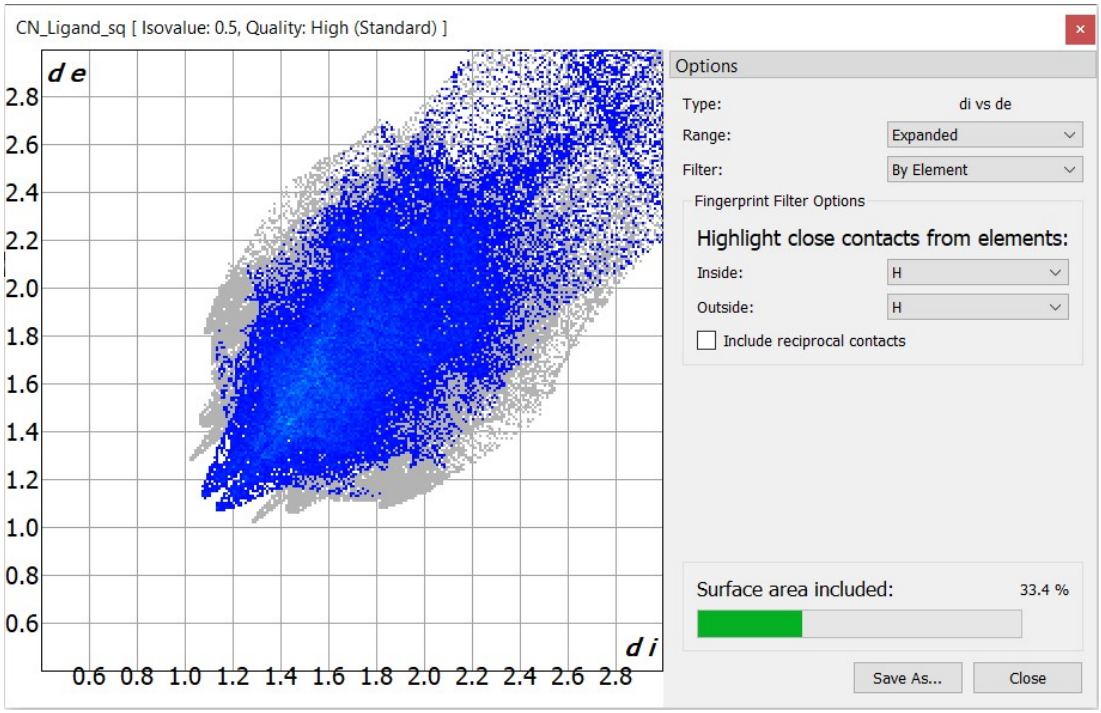

Fig. S51. Hirshfeld surface generated 2D fingerprint plot highlighting the relative contribution from H···H close contacts in the crystal structure of **P9**.

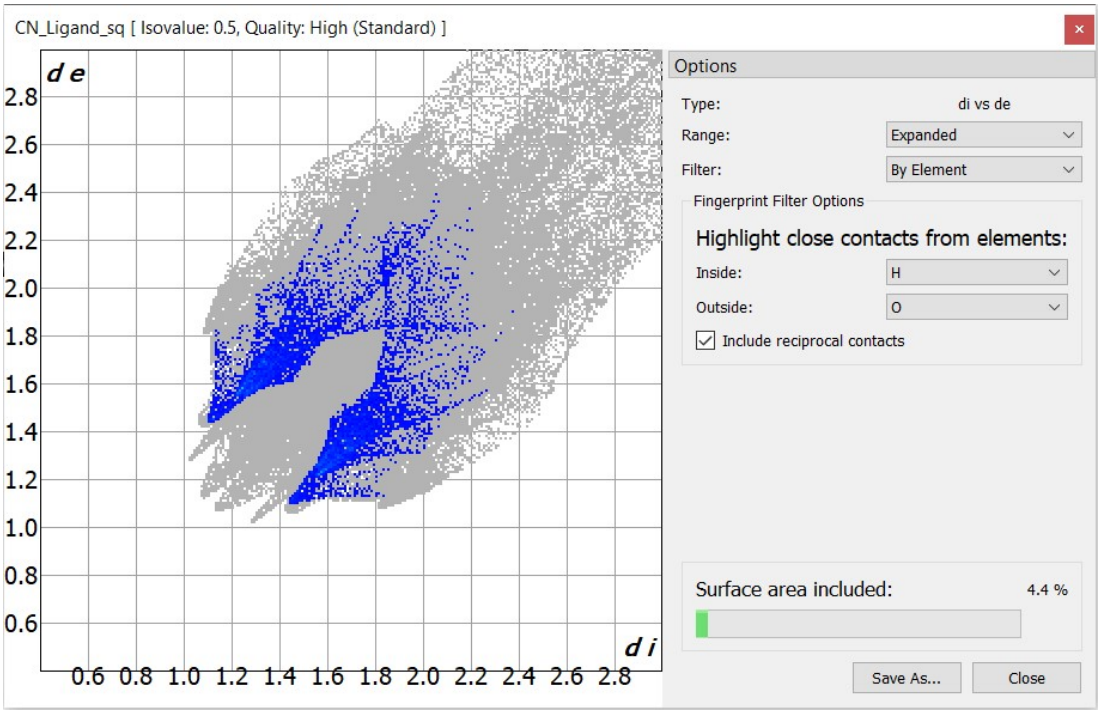

Fig. S52. Hirshfeld surface generated 2D fingerprint plot highlighting the relative contribution from H···O close contacts in the crystal structure of **P9**.

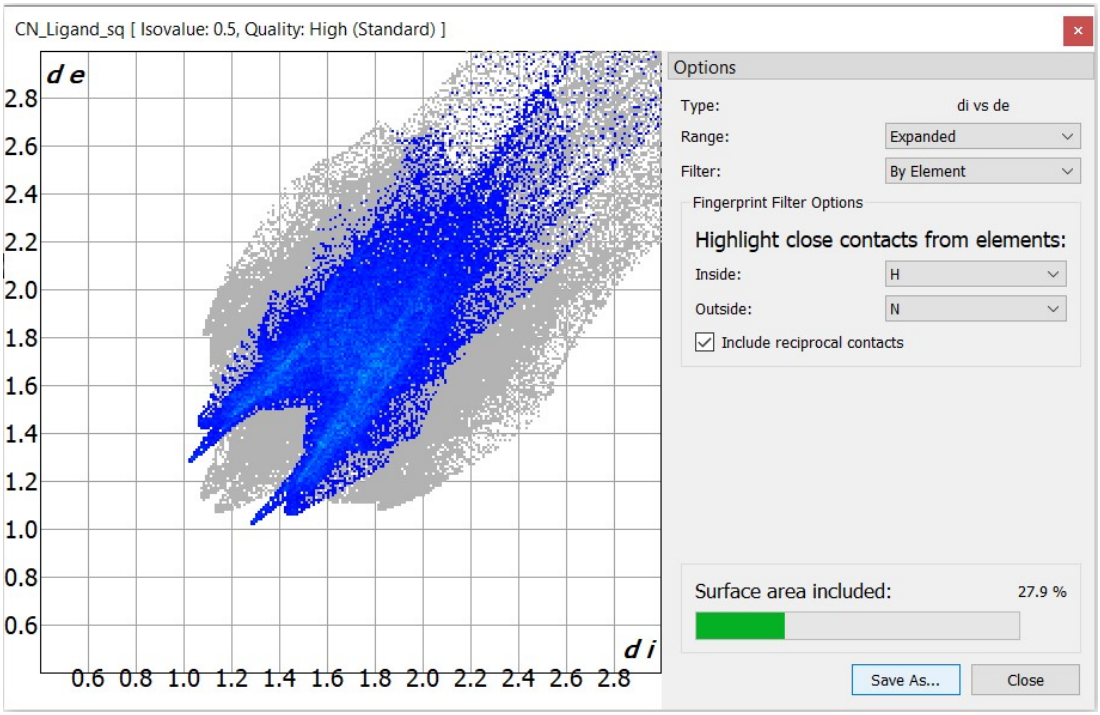

Fig. S53. Hirshfeld surface generated 2D fingerprint plot highlighting the relative contribution from H···N close contacts in the crystal structure of **P9**.

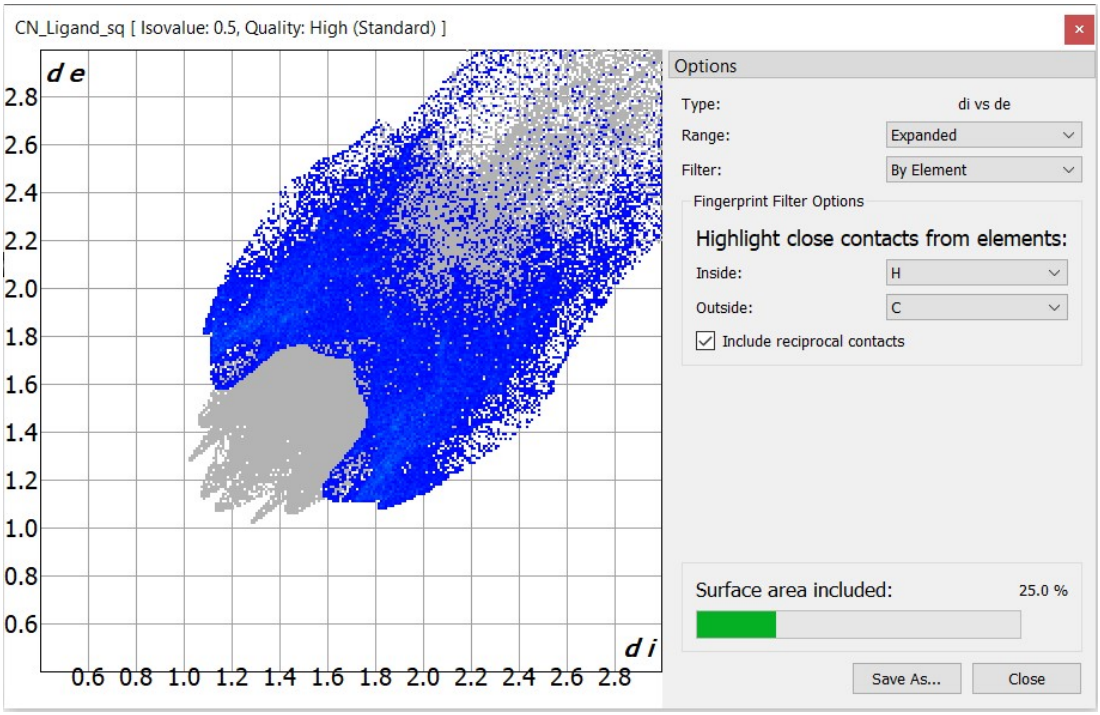

Fig. S54. Hirshfeld surface generated 2D fingerprint plot highlighting the relative contribution from H···C close contacts in the crystal structure of **P9**.

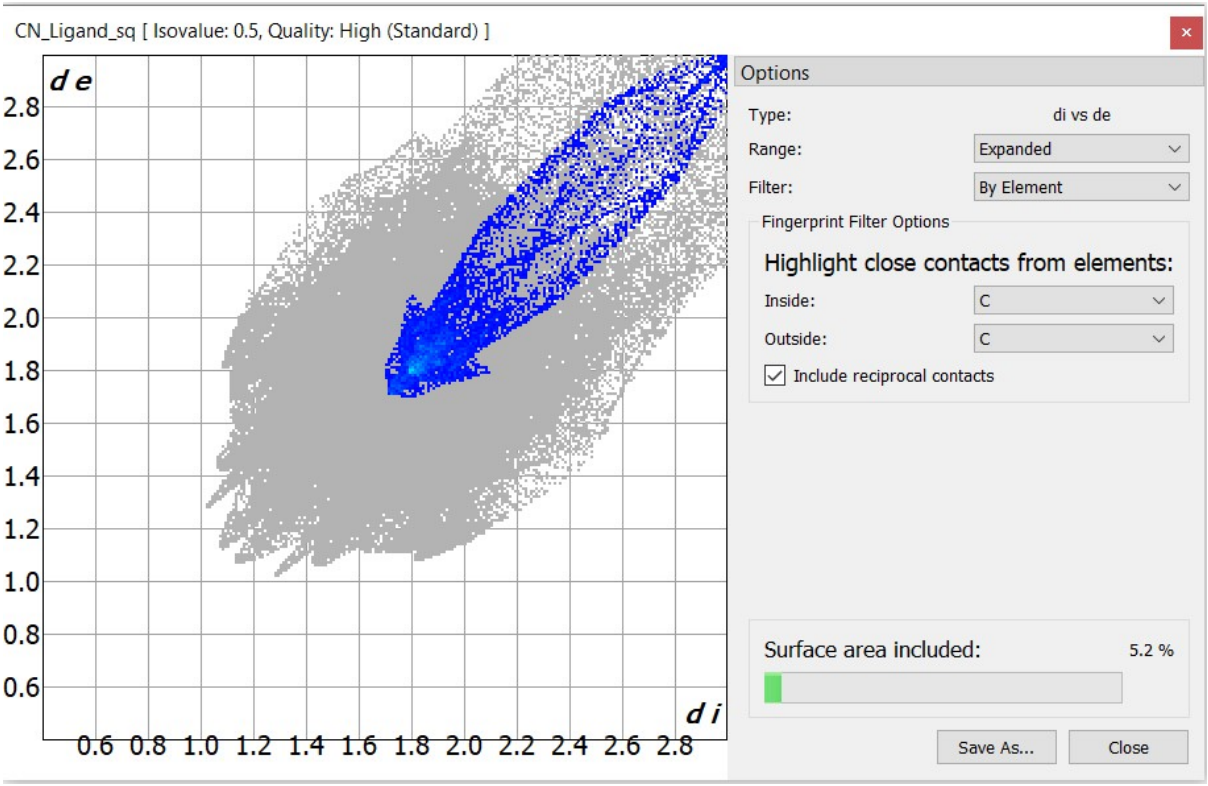

Fig. S55. Hirshfeld surface generated 2D fingerprint plot highlighting the relative contribution from C···C close contacts in the crystal structure of **P9**.

6. C-X···F⁻ and C-X···F⁻···H-F halogen bonding in solution (X = I/Br)

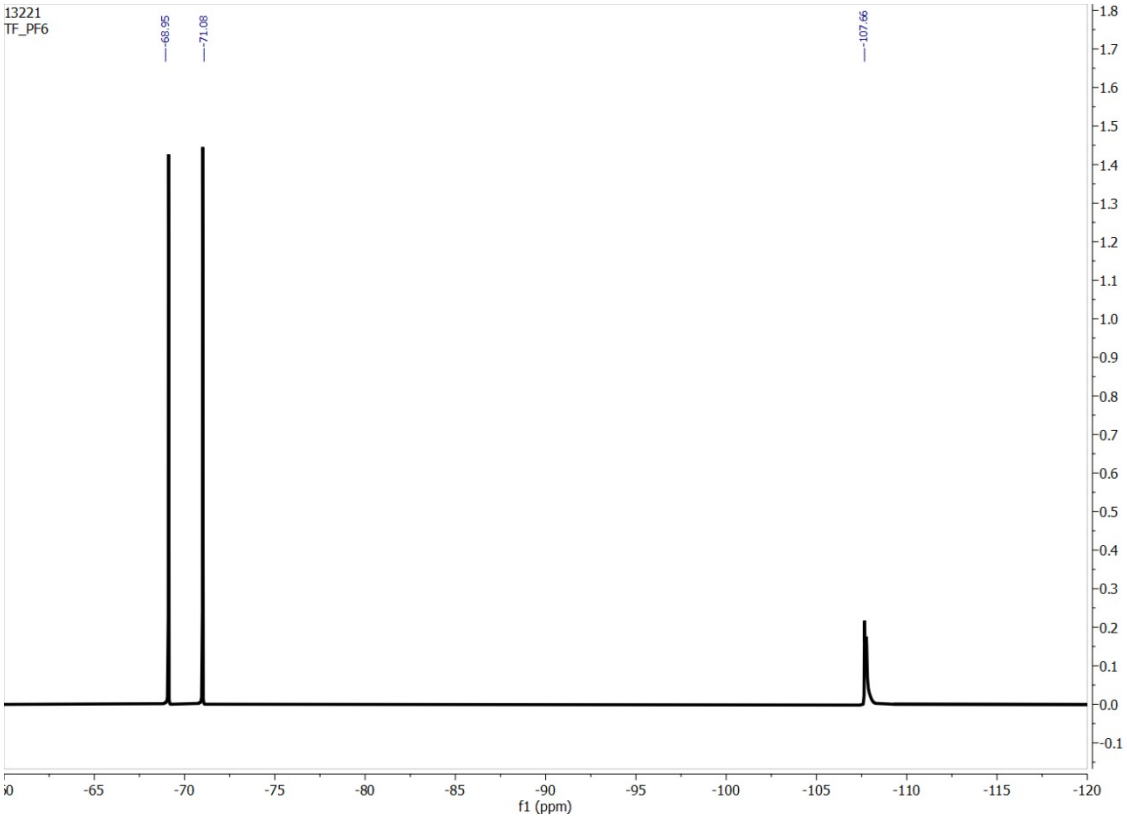

Fig. S56. ^{19}F NMR spectrum of $(Et)_4N^+F^-$ using $(n\text{-}Bu)_4N^+PF_6^-$ as a reference in DMSO-D_6.

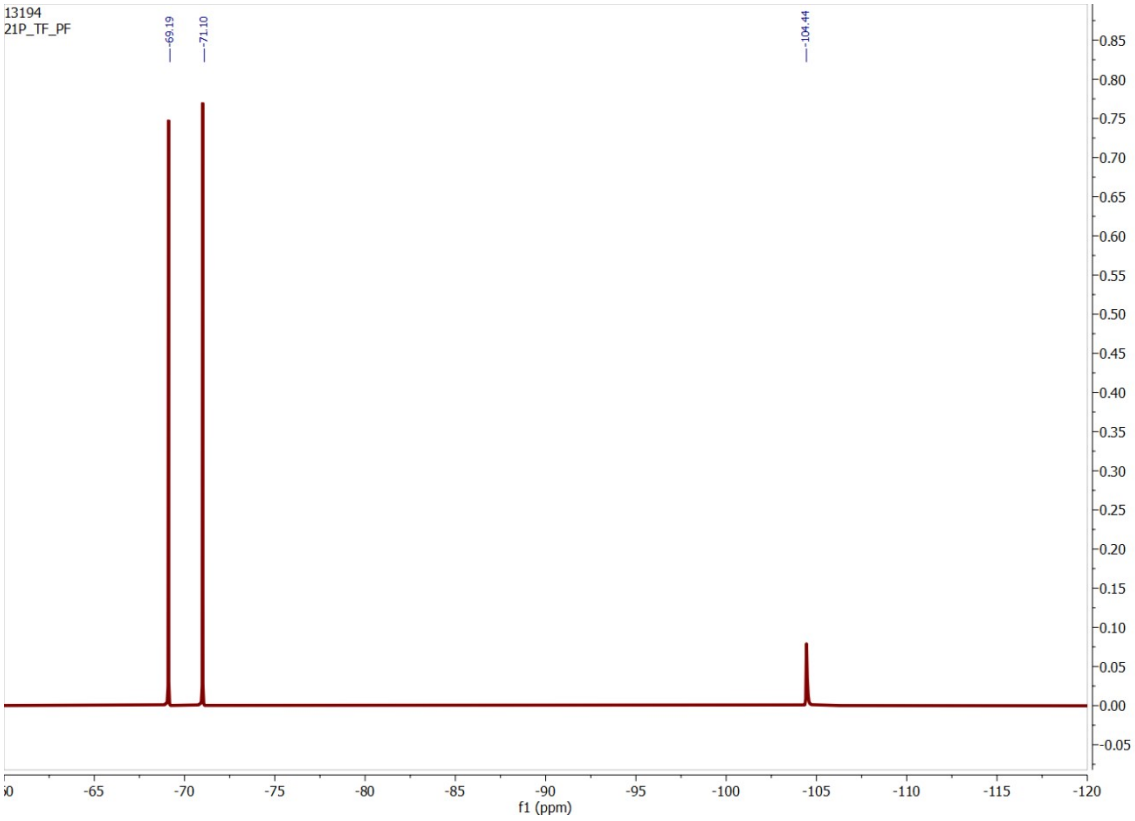

Fig. S57. ^{19}F NMR spectrum of $(Et)_4N^+F^-$ in the presence of equivalent amount of **P5** using $(n\text{-}Bu)_4N^+PF_6^-$ as a reference in DMSO-D_6. Fluoride signal appeared at −104.4 ppm.

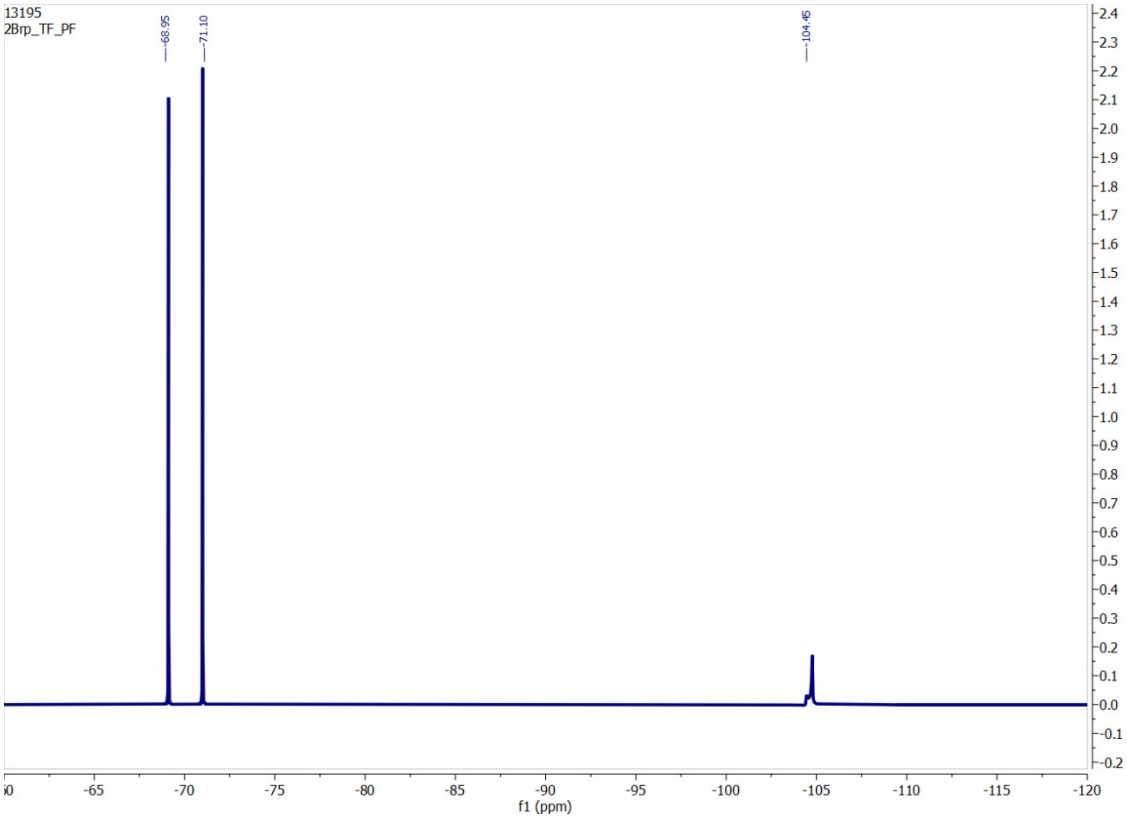

Fig. S58. ^{19}F NMR spectrum of $(Et)_4N^+F^-$ in the presence of equivalent amount of **P6** using $(n\text{-}Bu)_4N^+PF_6^-$ as a reference in DMSO-D_6. Fluoride signal appeared at −104.4 ppm.

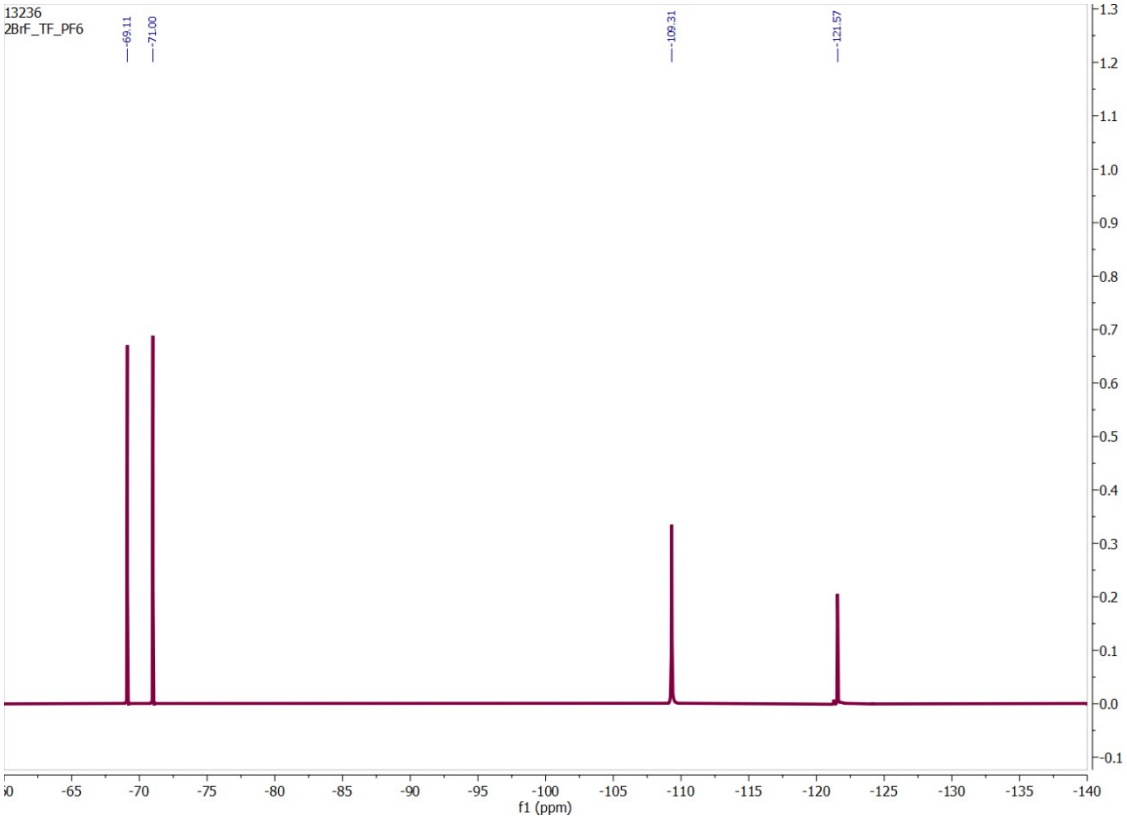

Fig. S59. ^{19}F NMR spectrum of $(Et)_4N^+F^-$ in the presence of equivalent amount of **P7** using $(n\text{-}Bu)_4N^+PF_6^-$ as a reference in DMSO-D_6. Fluoride signal appeared at −109.3 ppm and podand signal at −121.5 ppm.

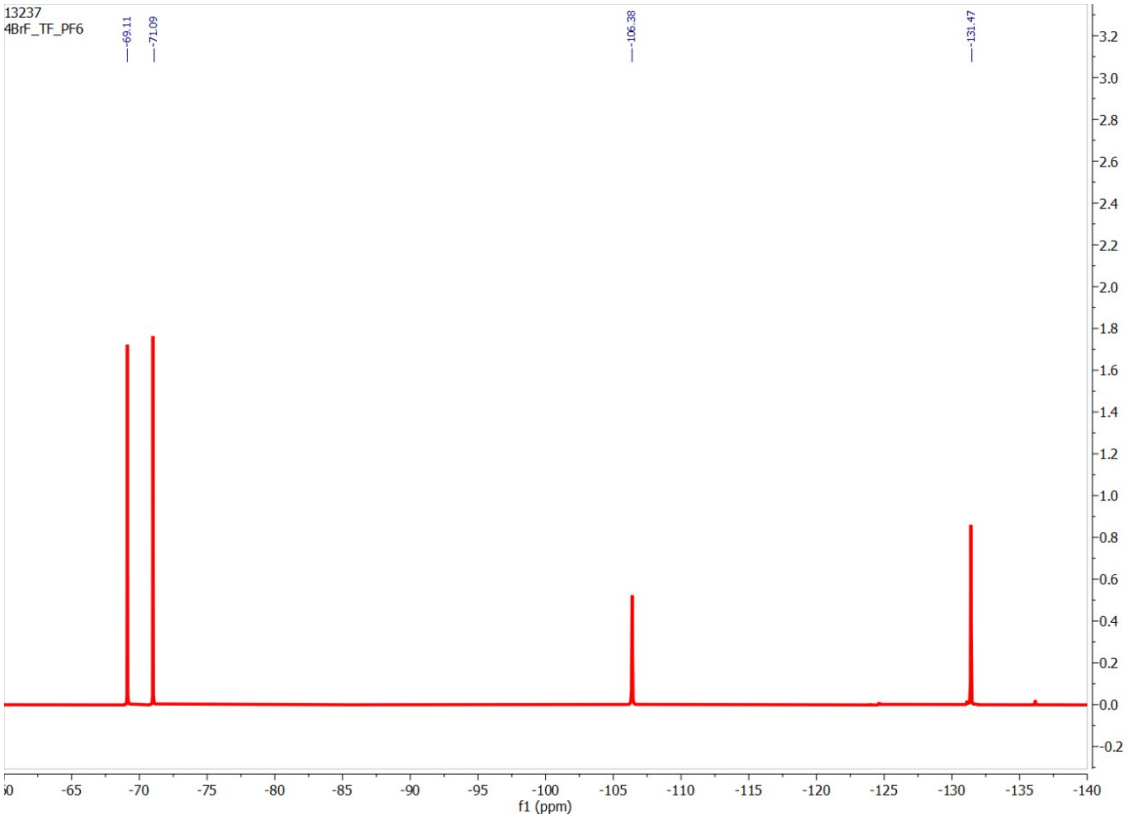

Fig. S60. ^{19}F NMR spectrum of $(Et)_4N^+F^-$ in the presence of equivalent amount of **P8** using $(n\text{-}Bu)_4N^+PF_6^-$ as a reference in DMSO-D_6. Fluoride signal appeared at −106.3 ppm and podand signal at −131.4 ppm.

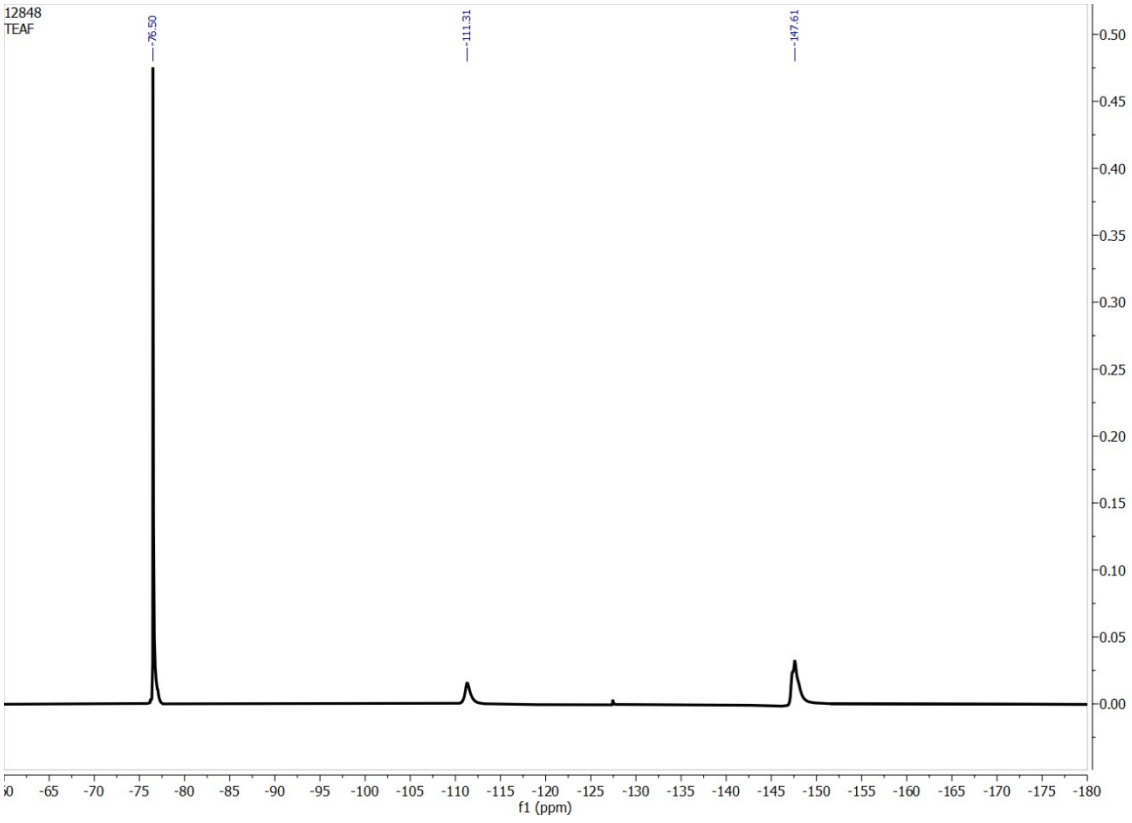

Fig. S61. ^{19}F NMR spectrum of $(Et)_4N^+F^-$ in the presence of trifluoroacetic acid (10 equiv.) showing the in-situ formation of hydrogen bifluoride, HF_2^- signal at −147.6 ppm in DMSO-D_6.

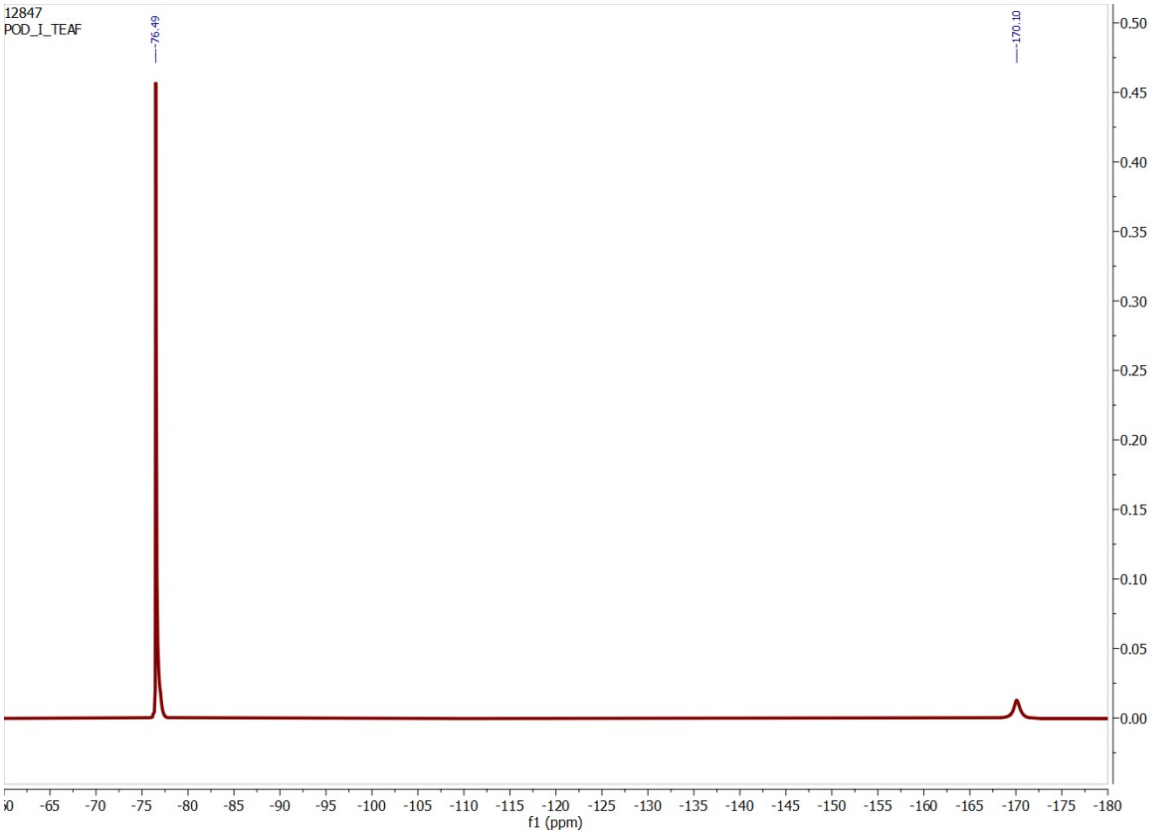

Fig. S62. ^{19}F NMR spectrum of $(Et)_4N^+F^-$ in the presence of equivalent amount of **P6** and 10 equiv. trifluoroacetic acid (reference) in DMSO-D_6. Hydrogen bifluoride signal appeared at −170.1 ppm.

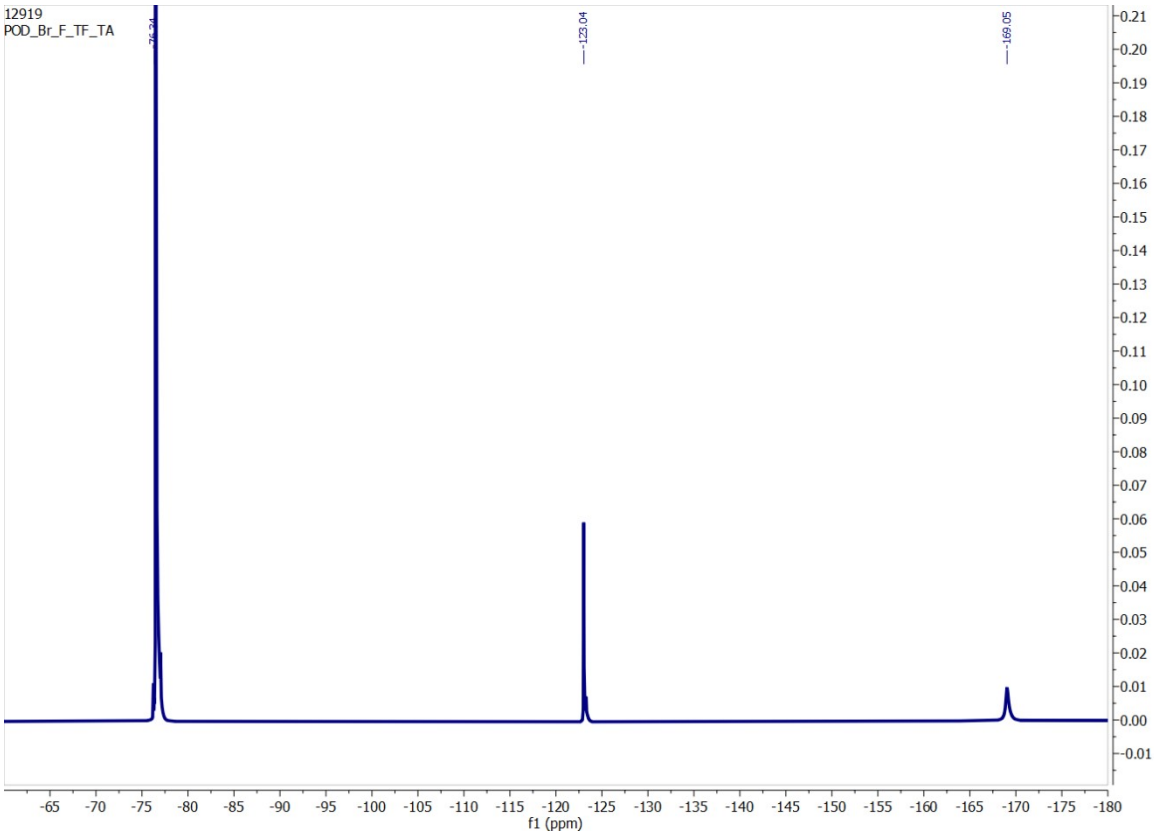

Fig. S63. ^{19}F NMR spectrum of $(Et)_4N^+F^-$ in the presence of equivalent amount of **P7** and 10 equiv. trifluoroacetic acid (reference) in DMSO-D_6. Hydrogen bifluoride signal appeared at −169.0 ppm.

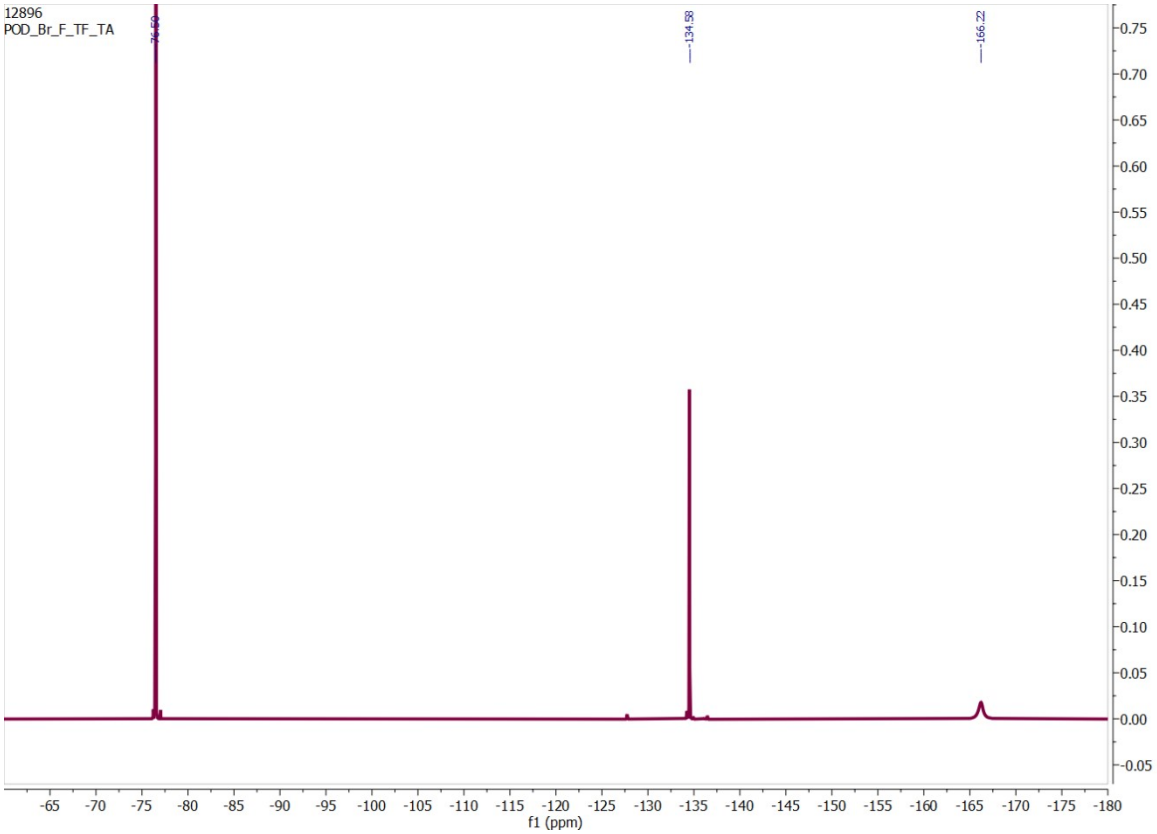

Fig. S64. ^{19}F NMR spectrum of $(Et)_4N^+F^-$ in the presence of equivalent amount of **P8** and 10 equiv. trifluoroacetic acid (reference) in DMSO-D_6. Hydrogen bifluoride signal appeared at −166.2 ppm.

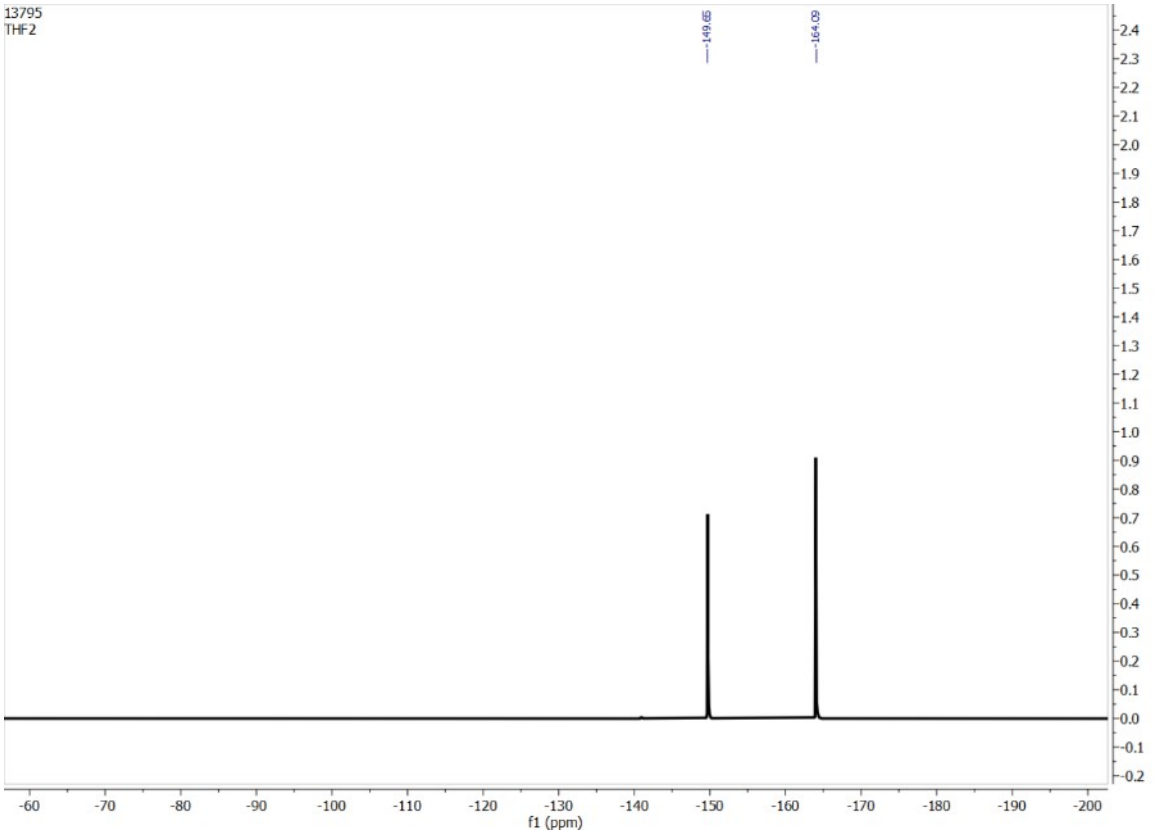

Fig. S65. ^{19}F NMR spectrum of $(n\text{-}Bu)_4N^+HF_2^-$ (HF_2^- signal −149.6) using hexafluoro-benzene a reference (C_6F_6 signal −164.0).

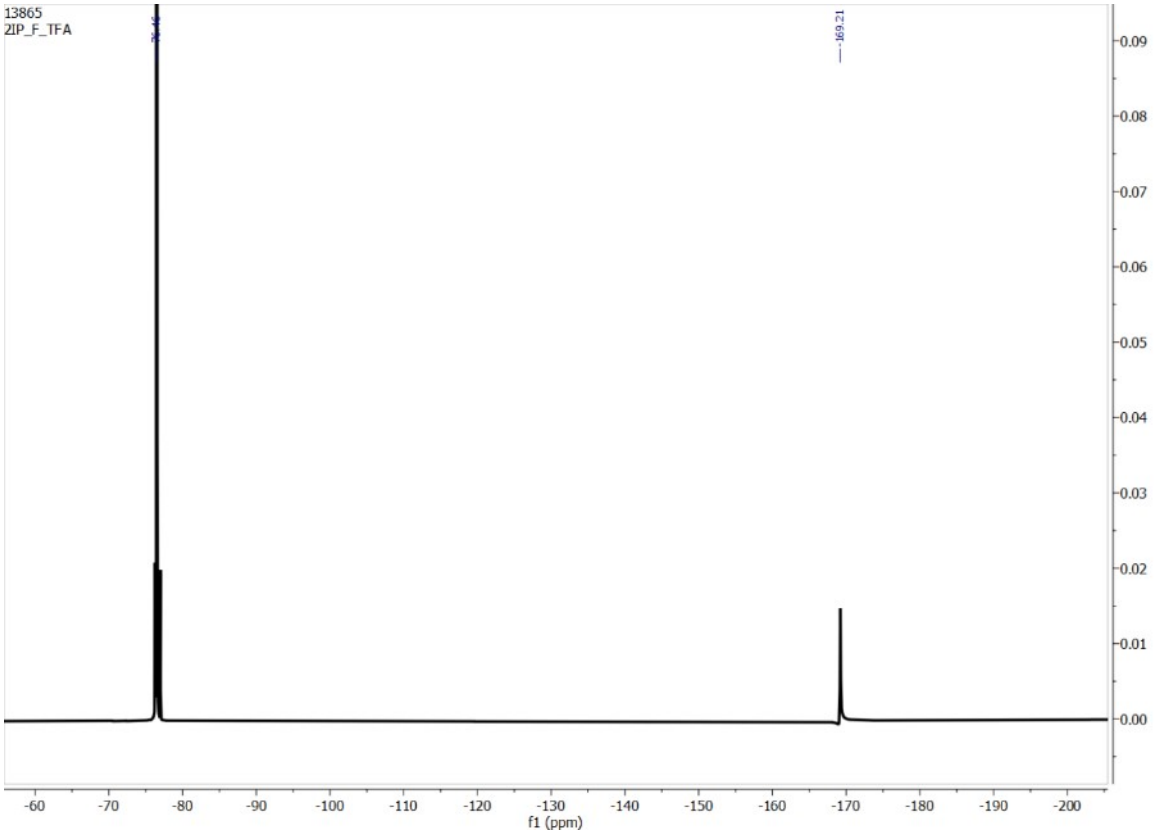

Fig. S66. ^{19}F NMR spectrum of $(n\text{-}Bu)_4N^+F^-$ in the presence of equivalent amount of **P5** and 10 equiv. trifluoroacetic acid (reference) in DMSO-D_6. Hydrogen bifluoride signal appeared at −169.2 ppm.

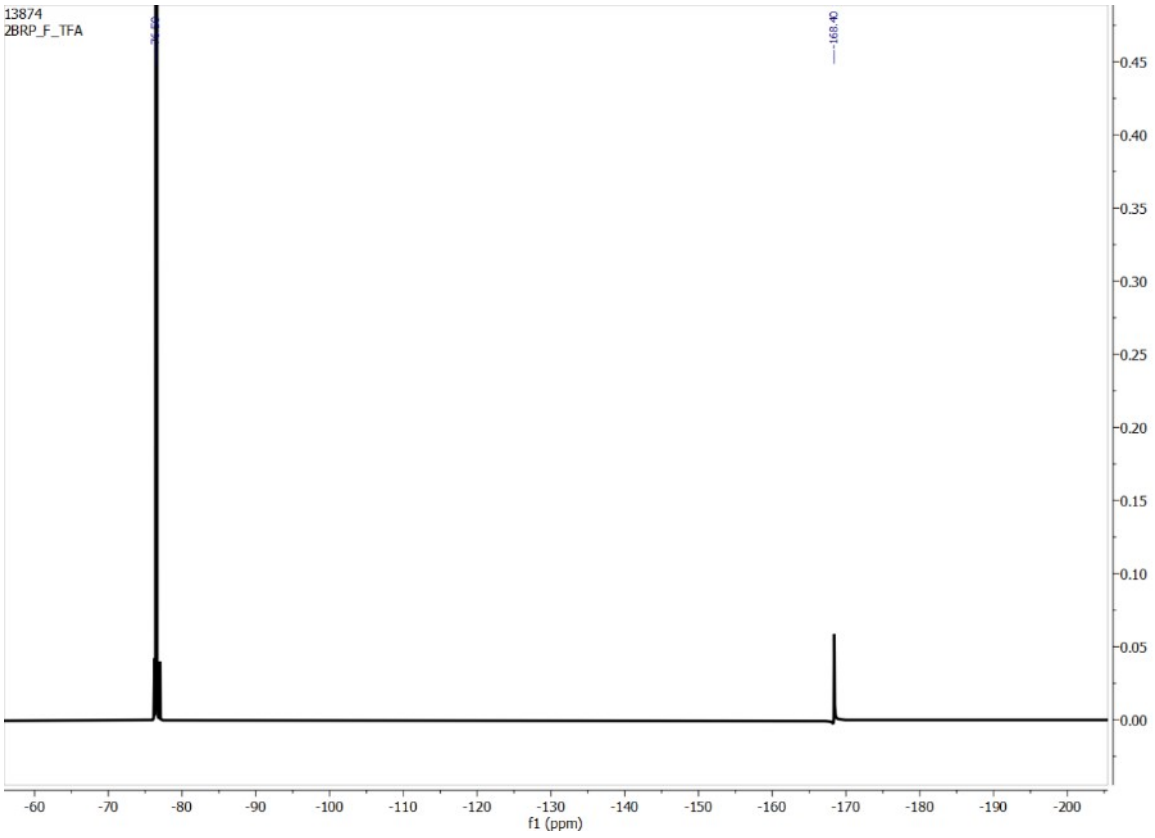

Fig. S67. ^{19}F NMR spectrum of $(n\text{-}Bu)_4N^+F^-$ in the presence of equivalent amount of **P5** and 10 equiv. trifluoroacetic acid (reference) in DMSO-D_6. Hydrogen bifluoride signal appeared at −169.2 ppm.